

This is a repository copy of *Tectonic evolution records closure of the Western Kunlun–Pamir Paleo-Tethys Realm: Insights from provenance analyses of Jurassic siliciclastic strata*.

White Rose Research Online URL for this paper: https://eprints.whiterose.ac.uk/id/eprint/232996/

Version: Accepted Version

Article:

Cui, H., Zhu, S., Mountney, N.P. orcid.org/0000-0002-8356-9889 et al. (6 more authors) (2025) Tectonic evolution records closure of the Western Kunlun-Pamir Paleo-Tethys Realm: Insights from provenance analyses of Jurassic siliciclastic strata. GSA Bulletin.

ISSN: 0016-7606

https://doi.org/10.1130/b38091.1

This is an author produced version of an article published in GSA Bulletin, made available under the terms of the Creative Commons Attribution License (CC-BY), which permits unrestricted use, distribution and reproduction in any medium, provided the original work is properly cited.

Reuse

This article is distributed under the terms of the Creative Commons Attribution (CC BY) licence. This licence allows you to distribute, remix, tweak, and build upon the work, even commercially, as long as you credit the authors for the original work. More information and the full terms of the licence here: https://creativecommons.org/licenses/

Takedown

If you consider content in White Rose Research Online to be in breach of UK law, please notify us by emailing eprints@whiterose.ac.uk including the URL of the record and the reason for the withdrawal request.



- 1 Tectonic evolution records closure of the Western Kunlun–Pamir
- 2 Paleo-Tethys Realm: Insights from provenance analyses of
- 3 Jurassic siliciclastic strata
- 4 Hang Cui^{1,2,3}, Shifa Zhu^{1,2,*}, Nigel P. Mountney³, Adam McArthur³, Jianzhou Tang⁴, Yao
- 5 Dong^{1,2}, Yihu Suo^{1,2}, Huan Tong^{1,2}, Xianzhang Yang⁵
- 6 ¹ National Key Laboratory of Petroleum Resources and Engineering, China University of
- 7 Petroleum (Beijing), Beijing 102249, China
- 8 ² College of Geosciences, China University of Petroleum, Beijing, 102249, China
- 9 ³ Sedimentology Research Group, School of Earth and Environment, University of Leeds, Leeds
- 10 LS2 9JT, UK
- 11 ⁴ College of Geology and Environment, Xi'an University of Science and Technology, Xi'an
- 12 710054, China
- 13 ⁵ Research Institute of Petroleum Exploration and Development, Tarim Oilfield Company,
- 14 PetroChina, Korla 841000, China
- *E-mail: sfzhu@cup.edu.cn.

ABSTRACT

16

17

- Determining the provenance history of Jurassic sediments in the south-western Tarim Basin
- 19 is crucial for deciphering the tectonic evolution of the Western Kunlun–Pamir Paleo-Tethys
- 20 Realm, which forms the north-westernmost segment of the Himalayan–Tibetan Plateau. Yet, the
- 21 detailed spatial provenance variation of these strata is poorly constrained. This study integrates
- field observations from three outcropping sections (cumulative thickness ca 6,800 m) and three

wells (ca 3,600 m) from four distinct regions (Qimgan, Oytag, Toyunduk–Kyzyltau, and Fusha). Samples were collected for sandstone petrology (n=54), heavy mineral assemblages (n=18), and detrital zircon U-Pb geochronology (n=10) to delineate the spatial difference in Jurassic provenance. The results indicate that the south-western Tarim Basin can be demarcated into two tectonic domains. 1) Detrital zircons in the Qimgan and Oytag regions were predominantly derived from nearby Triassic back-arc igneous rocks. Additionally, Late Paleozoic sub-populations were sourced from a bimodal volcanic sequence exposed in the north-eastern part of North Pamir, induced by Paleo-Tethys subduction. The North Pamir served as the main elevated source area, with negligible contribution from the Central or South Pamir. 2) The detrital zircons of Early Paleozoic and Neoproterozoic ages from the Toyunduk-Kyzyltau and Fusha regions predominantly originated from the North Kunlun-South Kunlun Terranes in response to Triassic collisional orogeny that induced significant uplift, effectively disconnecting the more distant provenance areas of the Tianshuihai/Songpan-Ganzi Terranes. Insights from provenance analysis permit the delineation of a refined geodynamic model for the tectonic evolution of the closure of the Western Kunlun–Pamir Paleo-Tethys Realm. Importantly, this study supports the hypothesis put forward in previous research, demonstrating Triassic back-arc volcanism in the northeastern Chinese Pamir. These findings not only deepen our insight into the tectonic evolution of the Western Kunlun-Pamir Paleo-Tethys Realm but also significantly enhance understanding on the dynamics of sedimentary basins, crustal development, and resource prospecting within convergent orogenic settings.

23

24

25

26

27

28

29

30

31

32

33

34

35

36

37

38

39

40

41

42

INTRODUCTION

44

45

46

47

48

49

50

51

52

53

54

55

56

57

58

59

60

61

62

63

64

65

66

The Himalayan-Tibetan orogen represents a composite terrane that was assembled through a series of collisional events and accretion along the southern periphery of the Asian continent (Fig. 1A), culminating in the present configuration between India and Eurasia (e.g., Windley, 1983; Kellett and Grujic, 2012; Metcalfe, 2021). Situated at the north-westernmost extent of the Himalayan-Tibetan Plateau, the Western Kunlun Shan-Pamir Realm (WKS-Pamir) has undergone a complex geodynamic evolution, characterized by the sequential origin, expansion, and closure of various branches of the Proto-, Paleo-, and Neo-Tethys Oceans. Evidence with which to reconstruct this evolutionary history is encapsulated in the remnant crustal fragments juxtaposed against a variety of volcanic arcs and suture zones (e.g., Gibbons et al., 2015; Liu et al., 2020; Tang et al., 2021), which provide critical insights into the origin and formation of Central Asia Orogen System. The region's significance surpasses its geological complexity. From a topographical and tectonic perspective, the contemporary WKS-Pamir epitomizes intracontinental collision and serves as a pivotal regulator of atmospheric composition exchange, thereby influencing regional and global climate patterns (e.g., Bershaw et al., 2012; Blayney et al., 2016). Understanding its geological history is thus essential for deciphering past climate dynamics. Despite considerable research devoted to the Cenozoic differential uplift history and the dynamic mechanisms of the WKS-Pamir (e.g., Sobel et al., 2013; Xu et al., 2021), its pre-Cenozoic tectonic evolution remains relatively poorly constrained. This knowledge gap is predominantly attributable to the profound overprinting of pre-Cenozoic geological processes by the Cenozoic tectonic evolution of the Pamir Plateau (e.g., Bershaw et al., 2012). Addressing this gap is vital for achieving a holistic

understanding of continental growth, basin evolution, and orogenic processes.

Research into the Mesozoic geodynamic history of the WKS-Pamir has focused on the genesis of igneous and metamorphic sequences exposed within or in proximity to sutures and plutons (e.g., Wang et al., 2020; Tang et al., 2021; Liu et al., 2023). Nevertheless, although the fieldwork may not be inherently difficult, the true challenge lies in the arduous process of securing permissions to conduct research in these areas, thus constraining the sampling of the majority of exposed terranes. The sediment factory – i.e., the system for the production of detrital material from bedrock and its subsequent transport to basins – retains characteristics that enable geologists to decipher information across the Earth's surface and interior. Such information includes the nature of the source rocks, tectonic setting, and modes of sediment transport, dispersal, and alteration (e.g., Johnsson, 1993; Weltje and von Eynatten, 2004; von Eynatten and Dunkl, 2012). The south-western Tarim Basin, bordering the north-eastern margin of the WKS-Pamir, hosts relatively continuous Jurassic sedimentary successions (Sobel, 1999), offering a prime opportunity to examine sedimentary provenance and decode the tectonic evolution associated with the closure of the WKS-Pamir Paleo-Tethys Realm. Nevertheless, Cenozoic crustal shortening and surface uplift have deformed the Jurassic sediments, restricting our ability to understand the form and origin of Jurassic tectono-sedimentary sequences (Schmidt et al., 2011; Sobel et al., 2013), their provenance, and highlight the need for further investigation. This study undertakes provenance analysis of Jurassic strata in the south-western Tarim

67

68

69

70

71

72

73

74

75

76

77

78

79

80

81

82

83

84

85

86

87

88

89

This study undertakes provenance analysis of Jurassic strata in the south-western Tarim Basin, the aim being to explain and discuss the tectonic evolution in the closure of the WKS-Pamir Paleo-Tethys Realm. To achieve this aim, this study presents results from a comprehensive investigation that integrates sedimentology (including field work and representative drill cores), thin section observation, heavy mineral signatures and detrital zircon U-Pb geochronology. The multifold objectives of this work are as follows: (1) to delineate the spatial characteristics of

Jurassic provenance differentiation; (2) to establish the tectonic setting of the Jurassic south-western Tarim Basin and elucidate the interplay between oceanic crust subduction, intracontinental collision, igneous activity, and sedimentary processes; and (3) to develop a refined model for the tectonic evolution of the WKS-Pamir Paleo-Tethys Realm closure.

This study imposes new constraints on the provenance and tectonic framework of Jurassic sequences, yielding critical insights into the broader geodynamic schema of the Paleo-Tethys and enriching our knowledge of intracontinental orogenic processes. The findings not only refine our grasp of the pre-Cenozoic evolutionary processes of the WKS-Pamir region but also exert significant influence on the comprehension of sedimentary basin evolution, crustal evolution, and resource exploration within convergent orogenic settings.

GEOLOGICAL SETTING

Regional Geology

The West Kunlun Shan

The West Kunlun Shan (WKS) forms a natural boundary between the Tarim Basin to the north and the Tibetan Plateau to the south (Fig. 1A), stretching *ca* 1,000 km along the southern margin of Laurasia (Xiao et al., 2003). Tectonically, the WKS is subdivided into the North Kunlun (NK), South Kunlun (SK), Tianshuihai, and Songpan–Ganzi Terranes (Fig. 1B, 2A).

The development of the WKS can be broadly categorized into three distinct stages.

1 Initial construction of the WKS occurred during the Early Paleozoic due to the subduction of the Proto-Tethys Ocean (Mattern and Schneider, 2000). The NK represents the southernmost uplift of the Tarim Block (Fig. 1B). This Paleozoic oceanic closure led to subduction between the Tarim Block and the Tianshuihai Terrane, forming the accretionary South Kunlun (SK) Terrane

- 113 (Xiao et al., 2003). The boundaries between these blocks are the Oytag-Kudi suture zone to the
- north of the SK (ca 526–494 Ma; e.g., Li and Zhang, 2014) and the Mazar-Kangxiwa-Subashi
- suture zone to the south (*ca* 487–485 and 455–446 Ma; e.g., Zhang et al., 2021; Zha et al., 2022).
- Extensive granitoid emplacement occurred in the NK (ca 440–410 Ma) and SK (ca 510–400 Ma),
- 117 reflecting Early Paleozoic collisional magmatism (e.g., Zhang et al., 2018; Yin et al., 2020). The
- Proto-Tethys Ocean's closure is accepted as ca 440–410 Ma, between the SK and NK Terranes
- 119 (Wu et al., 2020).
- 120 **2** The Late Paleozoic–Early Mesozoic was a crucial phase in WKS evolution, driven by Paleo-
- 121 Tethys Ocean subduction and the Cimmerian continent–Tarim Block collision (e.g., Graham et al.,
- 122 1993; Matte et al., 1996; Mattern and Schneider, 2000). In the Late Paleozoic, the northern
- periphery of Gondwana experienced the break-up of the continental crust along its margins
- 124 (Torsvik and Cocks, 2013; Xu et al., 2016). Concurrently, as the Cimmerian continent including
- the Songpan–Ganzi and Qiangtang Terranes (Fig. 1A) migrated northward, the Paleo-Tethys
- Ocean underwent rapid closure (Golonka and Bocharova, 2000). The Mazar-Kangxiwa-Subashi
- suture zone, south of the SK (Fig. 1B), marks the Paleo-Tethys Ocean's final closure (Liu et al.,
- 128 2020). The collision resulted in the emplacement of extensive granitoids, predominantly arrayed
- along both flanks of the Mazar–Kangxiwa–Subashi suture zone, with most intrusions dated to the
- 130 Triassic (e.g., Schwab et al., 2004).
- Throughout the Mesozoic, the WKS remained in a state of continuous uplift, with significant
- reactivation and uplift in the Late Mesozoic and Cenozoic, driven by Neo-Tethys Ocean closure
- and the Indian–Eurasian collision (e.g., Hendrix et al., 1992; Cao et al., 2015).
- The NK and SK are predominantly characterized by Precambrian metamorphic complexes,
- volcano-sedimentary successions, and unmetamorphosed carbonate-clastic sequences (Fig. 1B;

Zhang et al., 2019a). Abundant Paleozoic and Triassic granitoids are distributed along northwest—southeast-trending faults (Fig. 1B; e.g., Yuan et al., 2002; Wang et al., 2017; Yin et al., 2020). The Tianshuihai Terrane is primarily composed of Paleozoic and Mesozoic (metamorphosed) sedimentary rocks (e.g., Matte, et al., 1996, Cowgill et al., 2003; Luo et al., 2024). The Songpan—Ganzi Terrane mainly consists of Triassic and Jurassic plutons, and is accompanied by Triassic sedimentary rocks (e.g., Yin and Harrison, 2000; Xiao et al., 2007; Ding et al., 2013). The boundary between the Tianshuihai and the Songpan—Ganzi is commonly established along the Tanymas suture (Figure 1B and 2A); however, the details remain controversial.

The Pamir

Geographically, the Pamir adjoins the Alai Zone to the north and separates the Tarim and Tajik basins to the east and west, respectively (Fig. 2A). The Pamir is internally divisible into three principal terranes: the North Pamir (NP), Central Pamir (CP), and South Pamir (SP), which are demarcated by the Tanymas and Pashart suture zones, respectively (Fig. 1B; Schwab et al., 2004; Robinson et al., 2015; Song et al., 2024).

The NP represented the southern margin of Asia during the Late Paleozoic to Early Mesozoic (Aminov et al., 2023). The subduction of the Paleo-Tethys Ocean gave rise to extensive Carboniferous—Permian arc-like volcanic eruptions (Bazhenov, 1996; Song et al., 2024), including basalt, dacite, and volcanic breccia (Song et al., 2024). These volcanic rock assemblages are well exposed, accessible, and have been well dated in the Oytag region (Fig. 1B), which is bordered to the south by the Triassic Karakul granitoid batholiths (Rembe et al., 2022). Subsequently, the amalgamation of the NP, CP, and SP occurred, leading to the formation of extensive Triassic collisional granitoid batholiths (Karakul—Mazar) within the NP. Thus, the NP is predominantly composed of Paleozoic and Triassic sedimentary rocks, along with Carboniferous—Permian

volcanic rock assemblages and substantial Mesozoic granitoids (Fig. 1B; Schmidt et al., 2011; Blayney et al., 2016). Previous consensus suggested the Pamir domain migrated significantly due to Cenozoic northward indentation of the North Pamir (e.g., Burtman and Molnar, 1993; Cowgill, 2010). However, newer evidence points to a less extensive displacement (e.g., Chapman et al., 2017; Li et al., 2019b), with the Pamir salient's curvature likely due to plate boundary geometry rather than internal deformation (Li et al., 2020).

The convergence and eventual closure of the Paleo-Tethys Ocean between the NP and CP Terranes occurred in the Late Triassic, coinciding with the concomitant closure of the Rushan Ocean between the CP and SP, thus forming two suture zones, the Tanymas and the Pashart (Fig. 1B, 2A; Robinson, 2015). Subsequently, during the Cretaceous, the closure of the Shyok Ocean between the SP and Karakorum Terranes was marked by the emplacement of extensive granitoid intrusions within both terranes, spanning *ca* 130–95 Ma (Fig. 2A; e.g., Faisal et al., 2016; Aminov et al., 2017; Chapman et al., 2018b). The CP is characterized by a predominance of Paleozoic and Triassic–Jurassic clastic and carbonate successions, as well as Cenozoic orthogneiss (Fig. 1B; Schmidt et al., 2011; Hacker et al., 2017). Similarly, the SP Terrane is primarily composed of Paleozoic and Triassic–Jurassic strata, and extensive Cretaceous and Cenozoic magmatic rocks (e.g., Schwab et al., 2004; Robinson, 2015; Blayney et al., 2016).

Jurassic Stratigraphic System in the South-western Tarim Basin

The Tarim Basin constitutes a vast Mesozoic–Cenozoic intracontinental composite basin, superimposed upon a Paleozoic platform and Proterozoic metamorphic crystalline basement (Tian et al., 1989). It is positioned to the south of the Tien-Shan Mountains, north of the WKS, and is overthrust by the Pamir to the west (Fig. 1A).

The study area is located at the south-western Tarim Basin. The Triassic-Jurassic basin analysis of this region has been documented by Sobel (1999) and Wu et al. (2021, 2024), and hence, only a concise review is presented here. The Triassic tectonic setting was characterized by regional compression. A deformation belt, approximately 60 kilometers in width, characterized by fold-and-thrust structures, was established along the south-western margin of the Tarim Basin, which was precipitated by the collision of the Oiangtang Terrane with Eurasia (Fig. 1A). This collision led to substantial topographic uplift, meaning that there are few substantial and preserved accumulations of Triassic strata in the south-western Tarim Basin. Recent research has identified Triassic volcaniclastic strata exclusively within a few select sections, notably the Qimgan and Oytag Sections (Fig. 1C-D; Rembe et al., 2022). The Jurassic witnessed the formation of several narrow, deep, and discrete extensional grabens in the south-western Tarim Basin, stretching along the WKS-Pamir region, whereas the overlying Jurassic strata were sequentially deposited either upon the sparsely preserved Triassic strata, else upon the folded Paleozoic sequences. During the Jurassic, alluvial fan and intermontane river systems originating from the WKS-Pamir constituted the primary pathways for sediment supply, with ultimate deposition in a series of alluvial and lacustrine settings (Fig. 2B). The Jurassic sedimentation was predominantly governed by fault dynamics, which influenced regions and timing of sediment accumulation, and resultant stratal thickness variations.

Previous Provenance Studies of Jurassic Sedimentary Records

181

182

183

184

185

186

187

188

189

190

191

192

193

194

195

196

197

198

199

200

201

202

203

Sobel (1999) proposed that the depocenters of the Jurassic basins trended generally north-northwest, subparallel to the axis of the WKS-Pamir. The eastern flank of the Pamir and the westernmost portion of the Kunlun served as the principal elevated source area for Jurassic sediments. Bershaw et al. (2012) conducted detrital zircon analysis on one J₁s–J₂t clastic rock

sample from the Oytag section (Fig. 1D), revealing that the deposits were predominantly derived from Triassic igneous rocks. Zhang et al. (2019b) further supplemented detrital zircon analysis with one Jurassic J₃k sandstone sample from the Toyunduk–Kyzyltau section (Fig. 1E). They posited that, during the Jurassic, a westward-draining pattern evolved by headward erosion was established across the WKS and NP, with no significant contribution of detrital sediments from the CP and SP. Subsequently, Wu et al. (2024) undertook comprehensive field investigations of Jurassic strata in the Toyunduk–Kyzyltau and Kandilik sections (Fig. 1B). They conducted detrital zircon analysis on 3 samples from the J₁s–J₂t strata, and posited that there may be areas where the J₁s–J₂t strata are in parallel unconformable contact with the Jurassic J₃k strata, potentially leading to the variations in dynamics of its source-to-sink system.

METHODOLOGY

Sampling

In this study, our work focused on examination of three outcrops (Qimgan, Oytag and Toyunduk–Kyzyltau) and three wells (FS8, FS9 and KY1) in the south-western Tarim Basin, with 138 samples collected (Appendix A). Sampling sites were chosen to encompass the primary catchments that drained the surrounding mountains during the Jurassic (Fig. 1B). Sedimentological data, including composition, grain size, sedimentary structures, bedding geometry, and color, were recorded to delineate stratigraphic boundaries and define sedimentary facies. Subsequently, petrological and detrital zircon U-Pb analyses were conducted on 82 sandstone and conglomerate samples from J₁s–J₂t strata to differentiate Jurassic provenance. This research approach can mitigate the potential influence of provenance variations that may arise at the internal unconformable boundaries within the Jurassic (between J₂t and J₃k strata; Wu et al., 2024), thereby

minimizing the perturbing effects on the reliability of the results. Furthermore, the sandstones and conglomerates at the base of Jurassic, when contrasted with those at the upper portion, exhibit a greater capacity to preserve a more comprehensive set of information regarding the tectonic evolution of the orogenic belt.

This work collected U-Pb data on detrital zircons from modern river sands from previous publications to delineate the geochronological signature of the source area (Lukens et al. 2012; Carrapa et al. 2014; Blayney et al. 2016; Rittner et al. 2016; Liu et al., 2017). Utilizing modern river sands for terrane characterization is advantageous over using bedrock samples, as it offers a more representative average of a broader area (e.g., Blayney et al., 2016). It is crucial to emphasize that, despite the utility of modern river sand samples in charactering source area signals, significant biases are introduced due to factors such as the variable fertility of zircons, the sand generation potential of various lithologies, the distances of transport and the processes of recycling (Castillo et al., 2022). These elements can lead to the data being non-quantitatively representative across all scales. Therefore, this study adopts the observed distribution of U-Pb detrital zircon ages from modern rivers as a qualitative proxy that reflects the potential source regions, rather than as a precise quantitative measure.

Thin-Section Observation

Thin sections of 54 J₁s–J₂t samples were prepared to identify the detrital components within sandstones. Each thin section underwent blue-dyed epoxy impregnation and was stained with alizarin red-S solution to enhance the visibility and recognition of carbonate minerals. A point-counting procedure based on the Gazzi–Dickinson method was used to analyze the framework composition of sandstone samples. For each thin section, more than 300 points were counted. Only grains larger than 62.5 µm were included in the count. In addition to counting framework grains,

we simultaneously recorded the proportions of matrix, cement, and visible pore, when the microscope crosshair landed on areas outside the detrital grains. This expanded point-counting approach allows not only provenance interpretation through Q-F-L data, but also allows insights to be made regarding the diagenetic history of the sandstones (e.g.,). Grain size estimation in thin sections was conducted using a visual comparison method based on modal grain size ranges. Although semi-quantitative, this approach has been widely applied in petrographic studies due to its efficiency and reasonable accuracy (e.g., ****). The classification of sandstone grain size follows the standard scheme proposed by Folk (1980). Microscopic observations were performed with an Olympus BX51 metallographic microscope, utilizing both plane-polarized and crosspolarized light. The imaging system employed was the Olympus Stream, supplied by Olympus Soft Imaging Solutions GmbH. Detailed sample information and data can be found in Appendix B. The statistical petrographic data were represented on the Q-F-L and Lv-Lm-Ls diagrams (Garzanti, 2019) for petrographic classification.

Heavy Mineral Analysis

Heavy mineral analysis was performed on 18 J₁s–J₂t sandstone samples from outcrops characterized by alluvial-fan or river-delta facies. Approximately 20 grams of each sample were subjected to a series of treatments, including soaking in a 10% hydrochloric acid solution, grinding, panning with water, and drying. Following this process, particles ranging from 63–250 µm were selected as sub-samples (ca 5 grams). To separate the heavy mineral fraction, these sub-samples were treated with a tribromomethane solution with a density of 2.86 g/cm³. The separated heavy minerals were then mounted on 2 mm-thick glass slides with epoxy resin and identified using a Zeiss petrographic microscope (model Axio Imager A1). Minerals of possible authigenic origin, such as siderite and anhydrite, were also counted but were excluded from the detrital assemblage.

The raw counts of the remaining heavy mineral phases were normalized to sum to 100%, comparing the Jurassic provenance characteristics between different sections and wells.

In this study, we also employed the provenance-sensitive parameters GZI (Garnet Zircon Index) and ZTR (****) for comparative analysis of distinct source origins. The GZI is calculated as: GZI =100%× garnet/(garnet+zircon) (Morton and Hallsworth, 1994). The ZTR represents the cumulative percentage of ultrastable minerals, which includes zircon, tourmaline, and all phases of TiO₂ (Hubert, 1962). These parameters were computed and subsequently plotted to further evaluate the degree of scatter within the dataset.

Detrital Zircon U-Pb Geochronology

A total of 10 J₁s–J₂t rock samples (weighing ca 2 kilograms each) were disaggregated using an electric pulse disaggregation apparatus. The separation of detrital zircon fractions was accomplished through magnetic and heavy liquid separation techniques. A total of 250 zircons with diverse sizes and crystal habits were manually selected from each sample. The zircons were mounted in 25-mm epoxy discs and polished with 7000 mesh silicon carbide paper and 0.05-μm-diameter aluminum oxide to reveal the cores of the grains. Each mount was imaged using Cathodoluminescence (CL) to capture their internal textures. CL imaging was carried out with a TESCAN Mira 3 scanning electron microscope operating at an accelerating voltage of 7 kV, with an exposure time set to 2 minutes for clear image acquisition. Zircon grains with intact surfaces, varying size and shape, and absence of fluid inclusions were selected for analytical spot localization. A total of 120 spots were chosen for each outcrop sample, and 110 spots for each drilling sample as the final analytical targets.

For LA-ICP-MS analysis, zircon U-Pb dating was conducted at Beijing Quick-Thermo Science & Technology Co., Ltd., utilizing an ESI New Wave NWR 193^{UC} (TwoVol2) laser

ablation system coupled with an Agilent 8900 ICP-QQQ. The laser parameters were set to a spot size of 20 µm and a frequency of 5 Hz. The 91500 zircon standard was employed as the primary reference material for all U-Pb age determinations, with Plešovice zircon serving as the secondary reference (Sláma et al., 2008). Background subtraction and correction for laser-induced elemental fractionation were applied using the Iolite data reduction package within the Wavemetrics Igor Pro data analysis software (Paton et al., 2010). Detailed instrument conditions and experimental procedures are as described by Ji et al. (2020). Refer to Appendix C for a full description of the method. Probability density plots and peak ages were generated with ISOPLOT 4.15. The $^{206}\text{Pb}/^{238}\text{U}$ ratio was used for age determination of grains less than 1000 Ma, while the $^{207}\text{Pb}/^{206}\text{Pb}$ ratio was used for older grains. Data filtering was performed using standard discordance tests with a 10% threshold.

Multidimensional scaling (MDS) is a powerful technique for dimensionality reduction, widely applied in provenance analysis and the data mining of detrital zircon age datasets (Vermeesch, 2013; Stevens et al., 2013). The 3D-MDS plot generated by DZstats 2.30 (Saylor and Sundell, 2016) facilitates the clustering of Jurassic samples that share similar age spectra, while simultaneously differentiating those with distinct spectral characteristics. In this study, we employ a matrix of pairwise Euclidean distances to graphically represent and quantify the degree of similarity between each sample (Vermeesch, 2013).

STRATIGRAPHY AND PETROGRAPHY

Here, the stratigraphic and petrographic details of the three outcrops and three wells investigated are presented. The stratigraphic columns succinctly depict the principal stratigraphic

attributes of different formations. Appendix D collates the sedimentological attributes of each section and offers a concise interpretation of the depositional environments.

Qimgan Section

Field observations: The Jurassic strata in the Qimgan section is characterized by the continuous and excellent exposure of conglomerates, gravelly sandstones, and sandstones, intercalated with a minor occurrence of thin coal-bearing mudstone layers (See Appendix D for detailed explanations), with a total thickness of ca 1,950 meters (Fig. 3A). The earthy yellow and dark green andesitic conglomerate of the Triassic transitions abruptly upward into the purple-brown alluvial conglomerate of the J_1s , with a clear angular unconformity detected in the field. Conformable contact relationships are observed between the strata units within the J_1s – J_2t system, whereas a parallel unconformity contact relationship is noted within the J_2t – J_3k system and the Jurassic and the overlying Cretaceous strata (Fig. 3J). The J_1k and J_2y strata are characterized by interstratified gravelly sandstone, carbonaceous mudstone, and thin coal seams.

Petrography: The sandstones examined in the Qimgan section exhibits considerable complexity, but overall, they mainly plot within the fQL field on the Q-F-L diagrams (Fig. 4A). The framework component is Q_{34.0}F_{20.6}L_{45.4}, with an average matrix content of 7.1%. Quartz grains coa\mprise ~35% of the total framework grains, and are characterized by water-clear appearances, smooth surfaces, and sharply angular habits (Fig. 3F). Feldspars, including plagioclase and sanidine, are common and sometimes relatively abundant, but microcline is almost absent. The presence of oscillatory zoning and corroded embayment in plagioclase can be commonly observed (Fig. 3G). Lithics constitute an average of 45% and are primarily composed of mafic−intermediate volcanic rocks (Fig. 3H), with some granitoid and rhyolitic lithics present (Fig. 3I). All samples

plot closer to the Lv pole on the Lv-Lm-Ls diagrams, with an average composition of Lv_{80.8}Lm_{9.3}Ls_{9.9} (Fig. 4A).

Sandstones across a range of grain sizes did not exhibit significant differences in the composition of the framework and lithic components. Clastic grains of low chemical stability (e.g., plagioclase, basaltic lithics) preserve their original structural integrity and only exhibit a slight compaction-induced deformation. Examination of the thin sections reveals a paucity of dissolution features, with the majority displaying slight or no signs of cementation (Fig. 3 . .). Oytag Section

Field observations: Comparable to the Qimgan section, the Oytag section exhibits a similar Jurassic stratigraphy, predominantly composed of a well-preserved sequence of conglomerates and sandstones, which are occasionally interrupted by discrete layers of thin coal-bearing mudstones (Fig. 5A). Although the exposed thickness of the Jurassic strata is only ca 460 meters, the stratigraphic sequence is intact. The Jurassic strata initiates with the J₁s, characterized by earthy yellow conglomerates in faulted contact with underlying Triassic basalts (Fig. 5B). The section transitions upwards into earthy yellow and dark gray gravelly sandstone, interlayered with carbonaceous mudstone and thin coal seams in the J₁k and J₂y strata. The uppermost Jurassic strata consist of clast-supported conglomerate interbedded with dull red and grayish green mudstone. Petrography: The sandstones analyzed in the Oytag section collectively inhabit a transitional zone situated at the boundaries of five distinct fields (Fig. 4). However, in a stricter sense, medium-grained sandstones predominantly fall within the LQ field, whereas coarse-grained sandstones are more likely to be assigned to the fQL field, although the overall difference between the two is small (Fig. 4B). The framework component is

Q_{47.9}F_{12.0}L_{40.1}, with the average matrix content of 2.9%. The samples also collectively

exhibit a pronounced tendency to cluster near the Lv pole within the Lv-Lm-Ls diagrams, with the average composition of $Lv_{76.2}Lm_{13.0}Ls_{10.8}$ (Fig. 4B). The crystallographic and diagenetic characteristics of the various clastic grains exhibit a high degree of similarity to those of the Qimgan sandstones; thus, they aren't described again here. Toyunduk—

Kyzyltau Section

Field observations: The base of the Jurassic strata was inaccessible, leaving the underlying stratigraphic contact relationship undetermined for this section. However, regional geological mapping suggest that the Jurassic unconformably overlies Carboniferous strata (Fig.1E). The Toyunduk–Kyzyltau sequence begins with the J₁k strata, primarily consisting of taupe gray sandstones interlayered with carbonaceous mudstone and thin coal seams (Fig. 6A). The J₂y strata are characterized by the frequent interlayering of earthy-yellow rippled or horizontally burrowed siltstone and dark gray to black shale, which contain disseminated leaf fragments and thin coal beds (laterally continuous for thousands of meters, though part of the strata is obscured by Quaternary talus). The uppermost Jurassic strata predominantly feature laterally continuous dull red to grayish green siltstone interbedded with fine-grained sandstone and plant fossils, deposited throughout the J₂t strata, as well as dull red to purple brown massive conglomerate, deposited in the J₃k strata. The measured thickness of the Jurassic strata is ca 4,400 meters.

Petrography: The investigated sandstones in the Toyunduk–Kyzyltau section are predominantly categorized as quartzose and litho-quartzose (Fig. 4C), exhibiting an average composition of Q_{84.3}F_{0.9}L_{14.8}, with the average matrix content of 6.5%. The Toyunduk–Kyzyltau sandstones are distinguished by abundant quartz grains and the exceptionally low content of feldspar grains. Quartz grains consist primarily of monocrystalline grains (with an average of *ca* 72%) and polycrystalline grains (averaging *ca* 13%), typically exhibiting a sub-rounded

morphology with moderate sorting (Fig. 6H). The occurrence of cloudy and rough surfaces on individual quartz grains can be commonly observed. Lithics are predominantly composed of metamorphic (phyllite and schist) (Fig. 6I) and sedimentary lithics (siltstone). Metamorphic lithics collectively predominate over sedimentary lithics, and the proportion of volcanic lithics is significantly reduced compared to those in the Qimgan and Oytag sections (Fig. 4C). The average lithic composition is Lv_{6.7}Lm_{61.6}Ls_{31.7}. Variations in grain size did not correspond to notable changes in the proportions of framework component or lithic composition. It is noteworthy that the Toyunduk samples exhibit significant alteration of labile grains, particularly feldspars. Under compaction, some lithics and altered feldspars underwent plastic deformation and were squeezed into intergranular spaces, forming pseudomatrix (Fig. 4C; Galloway, 1974). The matrix is characterized by weakly aligned sericite flakes and silt-sized quartz and feldspars, features indicative of a metamorphic origin (schist or phyllite lithics), or from feldspar altered along cleavage planes. Given the inherent difficulty in reliably distinguishing protomatrix from pseudomatrix, a conservative approach was adopted, in which all matrix material was provisionally reassigned to either the metamorphic lithic or feldspar components, respectively. This approach yields a maximum estimate of (metamorphic) lithic and feldspar content, whereas the uncorrected values represent the minimum. Accordingly, the actual composition is expected to lie between these three parts, providing a more constrained basis for provenance and compositional interpretation (Fig. 4C). After matrix correction, the average framework components are Q_{78.4}F_{0.9}L_{20.7} (assigned to metamorphic lithics) and Q_{78.4}F_{7.6}L_{14.0} (assigned to feldspars), with the lithic composition comprising Ly_{5.7}Lm_{73.2}Ls_{21.1} (assigned to

metamorphic lithics). Fusha Region (Wells FS8, FS9 and KY1)

387

388

389

390

391

392

393

394

395

396

397

398

399

400

401

402

403

404

405

406

407

408

409

Observations: In Well FS8, the Jurassic strata are ca 1,700 meters thick (Fig. 7A). The basal Jurassic is comprised of conglomerate and sandstone interbedded with siltstone, with a thickness of ca 300 meters (all sampling and analysis in this well were focused in this interval). The strata transition upward into gray to black mudstone, with a few relatively thin intercalations of siltstone, sandstone, coal seams, and plant fossils, reaching a thickness of ca 1,400 meters. Well FS9 also hosts Jurassic strata of ca 1,700 meters in thickness (Fig. 7B), with similar stratigraphic contact relationship and vertical lithologic characteristics with Well FS8. The notable difference is that the basal coarse-grained deposits in Well FS9 are only ca 30 meters thick. In Well KY1, the Jurassic strata are ca 200 meters thick (Fig. 7C). The lower half is predominantly conglomerate with a few relatively thin intercalations of finer-grained sediments. As the proportion of gravel decreases towards the upper half, a significant phase of coal seam deposition occurs, accompanied by the continuous deposition of sandstone and conglomerate.

Petrography: All samples in the Fusha Region plot within LQ fields (Fig. 4D), with a mean framework component of Q_{74.1}F_{3.5}L_{22.4}. The average matrix content is 6.1%. The quartz grains consist of monocrystalline grains (averaging *ca* 61%) and polycrystalline grains (averaging *ca* 14%). Lithics predominantly consist of chert and high-grade metamorphic lithics (Fig. 7E–G). The content of volcanic lithics, which averages *ca* 5%, is notably lower compared to the Qimgan and Oytag sections. All samples plot closer to the Lm pole on the Lv-Lm-Ls diagrams, with the average composition of Lv_{21.6}Lm_{50.2}Ls_{28.2}.

The crystallographic and diagenetic characteristics of the various clastic components and matrix exhibit a high degree of similarity to those of the Toyunduk sandstones; thus, they are not described again here. A comparable approach to matrix correction was likewise implemented for the sandstones in this region (Fig. 4D). After matrix correction, the average framework

components are Q_{69.4}F_{3.3}L_{27.3} (assigned to metamorphic lithics) and Q_{78.4}F_{9.6}L_{21.0} (assigned to feldspars), with the lithic composition comprising Lv_{16.4}Lm_{61.8}Ls_{21.8} (assigned to metamorphic lithics).

Depositional Age

The presence of coal seams in the south-western Tarim Basin is proposed as a possible proxy for the Jurassic system (Zhong et al., 2002); though limited by the lack of chronological data, it retains an indicative value. Approximately 30 kilometers northeast of the Oytag section, Liu et al. (2002) undertook a detailed pollen analysis on two samples derived from the J₂t strata (Appendix E). The analysis indicated a prevalence of *Cyathidites minor*, *Classopollis annulatus*, *Pseudopicea variabiliformis*, and *Abietineaepollenites pectinellus*, which collectively suggest a stratigraphic age spanning from the Triassic to the Early Cretaceous.

In the absence of a precise depositional age for the Jurassic strata of the south-western Tarim Basin, the following evidence suggests a depositional period ranging from the Toarcian to the Bathonian. (1) Rb-Sr dating of red rhyolitic crystal tuffs located approximately 40 kilometers south-west of the Oytag section yielded an age of 180 ± 10 Ma (Arnaud, 1992). The presence of similar volcanic detritus within the Jurassic basal conglomerates at the Oytag section suggests a maximum depositional age that is approximately contemporaneous with the Toarcian (Sobel, 1999). (2) Approximately 50 kilometers north of the Qimgan section are outcrops of sandstone-hosted copper deposits in J_3k sedimentary rocks, Sarekebayi sub-basin. The chalcopyrite has been dated to 166.3 ± 2.8 Ma using the Re-Os geochronometric method (Fang et al., 2018), indicating a minimum depositional age that is approximately coeval with the Bathonian.

HEAVY MINERAL ASSEMBLAGES

The relative percentages of heavy minerals in sandstone samples are plotted as a heatmap for optimal clarity (Fig. 8). Overall, the most prevalent heavy minerals are ilmenite, zircon, tourmaline, and garnet, present in 100%, 100%, 72.2%, and 61.1% of the analyzed samples, with median concentrations of 67.9%, 20.5%, 3.4%, and 2.5%, respectively. Other transparent heavy minerals include rutile, apatite, epidote, and titanite.

The heatmap, MDS plot, and tourmaline-garnet-epidote triangular diagram of the heavy mineral assemblages has identified two primary clusters, A (comprising the Qimgan and Oytag sections, n=6) and B (comprising the Toyunduk–Kyzyltau section and Fusha Region, n=12) (Fig. 8A–C). These clusters exhibit pronounced differences in the proportions of ilmenite, tourmaline, garnet, and epidote. Samples in cluster A display relatively low ilmenite content (6.3%–67.6%, with a median of 47.9%), with relatively higher concentrations of garnet (8.8%–34.4%, with a median of 16.6%), as well as a minor but notable presence of epidote. Samples in cluster B exhibit a relatively high concentration of ilmenite, ranging from 6.3% to 67.6% with a median of 47.9%, and contain varying proportions of tourmaline, from 2.1% to 15.2% with a median of 6.0%, while garnet is scarcely detectable. In terms of heavy mineral indices, samples in cluster A contained GZI values ranging from 18.9 to 55.2 and ZTR values from 20.7 to 57.8, whereas samples in cluster B possessed GZI values from 0 to 24.0 and ZTR values from 8.8 to 31.7, both significantly lower than those of samples in cluster A (Fig. 8D–E).

DETRITAL ZIRCON U-PB GEOCHRONOLOGY

Zircon Morphologies and Th/U Ratios

A total of 2,500 zircon grains were extracted from 10 sandstone samples for morphological characterization, and 1,150 representative grains were selected for subsequent element analysis and U-Pb dating. The zircon grains exhibited a range of sizes, with cross-sectional diameters predominantly between *ca* 60 and 300 μm. The smaller grains tended to be equant, whereas the larger grains were typically elongated, reaching maximum aspect ratios of 1:5. The majority of zircon grains displayed a stubby prism morphology with angular to sub-angular features. CL imaging revealed that most zircons exhibited oscillatory, sector, or irregular concentric internal zoning, which was occasionally truncated by a new or recrystallized growth zone (Fig. 9), indicative of an igneous origin (Corfu et al., 2003). Approximately 10% of the fraction of zircons present a lighter color and exhibits either weak oscillatory zoning or metamorphic accretion textures, such as those observed in Figure-9C-#70 and Figure-9E-#48, among others.

The Th/U ratios of the detrital zircons from the Jurassic strata spanned from 0.02 to 6.67, with a concentration of values between 0.2 and 1.3 (Fig. 10). A significant proportion of the grains, 82.1% (944 out of 1,150), had Th/U ratios greater than 0.4, suggesting that these zircons originated from igneous protoliths (e.g., Corfu et al., 2003; Linnemann et al., 2011). Only 10 zircons out of the 1150 grains that presented Th/U ratios of <0.1, are interpreted to be aqueous fluid-precipitated overgrowths or metamorphic in origin (Liati et al., 2002; Grant et al., 2009). Certainly, Th/U ratios <0.1 do not entirely preclude the possibility of magmatic growth, especially where modest degrees of partial melting lead to relative enrichment of U over Th (Williams, 2001).

Detrital Zircon U-Pb Geochronology

The detrital zircon U-Pb age data from 27 modern-river samples (Figs. 11) and 10 J_1s-J_2t sandstone samples (Figs. 12) are presented as percentage components in probability density plots (PDP) and pie charts (Figs. 12). To evaluate the spatial variation in Jurassic provenance, this work

also compiled detrital zircon U-Pb data from previous studies for four J₁s–J₂t samples: one from the Oytag section (Bershaw et al., 2012) and three from the Toyunduk–Kyzyltau and Kandilik sections (Figs. 12; Wu et al., 2024).

For the sample QM-Z1, the majority of zircon grains cluster between *ca* 250 and 225 Ma, with a prominent peak at 235 Ma. Additionally, minor age populations between 1,000 and 600 Ma are discernible. The detrital zircon of the sample QM-Z2 analyses revealed a range of ages from 2,893 to 227.1 Ma, with the dominant ages being Triassic (*ca* 240–227 Ma, with a major peak at 233 Ma), and subordinate ages being Neoproterozoic (*ca* 680–600 Ma and 1,000–930 M). The sample QM-Z3 contains a prominent group of detrital zircons aged to *ca* 240–215 Ma, with a peak at 223 Ma, as well as two individual sub-populations ranging from *ca* 450–420 Ma and 950–800 Ma.

Two sandstone samples, OY-Z1 and QY-Z2, were collected from the Oytag section (Fig. 5A), exhibiting slightly distinct age distributions (Fig. 12). The predominant age populations of the sample OY-Z1 are distributed between *ca* 260–200 Ma, with a notable peak at 226 Ma, and another significant grouping between *ca* 450–385 Ma, culminating at 399 Ma. Additional minor age clusters are observed at *ca* 300 Ma and 331 Ma. The sample OY-Z2 predominantly displays the age populations of Triassic and Early Paleozoic, featuring a pronounced peak at 251 Ma, and two subordinate peaks at 302 Ma and 351 Ma. Furthermore, the sample PMR-25 from a previous study (n=86; Bershaw et al., 2012) exhibits age patterns broadly congruent with those of the sample OY-Z2.

In the Toyunduk–Kyzyltau and Kandilik sections (Fig. 1B), the available data sets for the J_1s-J_2t strata are provided by Wu et al. (2024), and hence, only a concise review is presented here. The age distributions of detrital zircons exhibit strikingly consistent population patterns,

characterized by main peaks in the Early Silurian (*ca* 450 Ma) and Tonian (*ca* 800 Ma) age. This similarity suggests that the sediments from the two outcrops originated from a common exhumed provenance (Wu et al., 2024).

Five sandstone samples, designated as FS8-Z1, FS8-Z2, FS9-Z1, KY1-Z1, and KY1-Z2, were extracted from three wells in the Fusha Region (Fig. 7A–C), exhibiting largely consistent age patterns (Fig. 12). The zircon age spectra of the samples FS8-Z1 and FS8-Z2 reveal a straightforward pattern with primary age peaks concentrated *ca* 480–420 Ma and 850–750 Ma. Moreover, both samples contain a minor yet significant proportion of Mesozoic, Mesoproterozoic, Paleoproterozoic, and Archean zircons. The sample FS9-Z1 is characterized by a high abundance of Paleozoic (*ca* 460–410 Ma) and Neoproterozoic (*ca* 850–730 Ma) zircons, with notable peaks at 430 Ma and 784 Ma. It also includes a minor but noteworthy component of Mesoproterozoic, Paleoproterozoic, and Archean zircons. The samples KY1-Z1 and KY1-Z2 exhibit a pronounced unimodal age peak at *ca* 450 Ma, accompanied by a distinct subpopulation that peaks at *ca* 820 Ma (Fig. 12).

PROVENANCE INTERPRETATION

Thin Section Observation Aspect

The mean framework components, lithic compositions, and optical characteristics of the sandstones within the Qimgan and Oytag sections exhibit a significant similarity (Fig. 4). Such intimate correspondence suggests a considerable degree of provenance similarity. The presence of well-preserved volcanic lithics suggests that diagenetic processes have exerted only a minor influence on the original composition of the rock (Panca et al., 2024). The irregularly shaped quartz crystals with sharp edges and corroded embayments suggest a volcanic origin, which is atypical

of most fluvial or eolian terrigenous detritus (Fig. 3A, 5A; Bohor and Tripleborn, 1993). The latter typically exhibit significant sorting and rounding characteristics, along with a blurred surface texture. The oscillatory zoning and corroded embayments in plagioclase and the widespread occurrence of volcanic lithics are also definitive hallmarks of a volcanic provenance (Fig 3F-I, 5F–I; Pittman, 1970), although oscillatory zoning of plagioclase can also be found from granitoid sources. Given the widespread occurrence of mafic volcanic lithics and the relatively low abundance of granitoid lithics, the North Pamir Triassic granitoids are unlikely to have been the dominant source, but may have provided a minor contribution to the sediment supply (Fig. 1B). Accordingly, the evidence presented leads us to favor the interpretation of the provenance as being of volcanic origin. For the Toyunduk-Kyzyltau section and Fusha regions, following matrix correction, all data points predominantly plot within the fLQ, LQ, and Qu fields, likely reflecting the source characteristics of schists and paragneisses (Garzanti et al., 2010). The substantial number of quartz grains and the prevalence of metamorphic lithics (phyllite, schist and gneiss) and mica imply that the provenance is largely attributable to a metamorphic or granitoid source (Fig. 4C–D, 6-7), markedly divergent from the characteristics exhibited by the parent volcanic rocks of the Qimgan and Oytag sections. This suggests that the sandstones in the region may be linked to the provenance supply from metamorphic complexes and granitoids of the WKM (Fig. 1B). This region potentially harbors a minor fraction of recycled sedimentary rocks (Fig. 4C), which implies a complex evolutionary history characterized by crustal recycling and deformation processes. The occurrence of cloudy and rough grain surfaces may indicate that the transportation was slightly longer compared to the Qimgan and Oytag samples; yet, the overall structural maturity of the rock remains relatively low. The enhanced diagenetic alteration is considered a plausible explanation for the diminished feldspar content observed within the rocks. Following this alteration, the

546

547

548

549

550

551

552

553

554

555

556

557

558

559

560

561

562

563

564

565

566

567

568

feldspar grains experienced a marked reduction in compaction resistance, which ultimately resulted in their transformation into the pseudomatrix.

Although grain-size variations are observed among the sandstones, the framework component and lithic composition remain broadly consistent when compared within each individual region (Fig. 4). This may be attributed to the proximal, high-energy depositional setting—alluvial fans and braided river deltas (Appendix D)—where two factors contribute to compositional similarity across grain-size fractions: (1) a compositionally uniform and stable source area that strongly controlled sediment supply; (2) unlike distal marine settings, the alluvial fan and braided river delta systems in the study area were characterized by relatively rapid sedimentation rates. Such sediments are typically eroded, transported, and deposited over short distances, resulting in frequently fluctuating hydrodynamic conditions but insufficient time and spatial extent for effective mineralogical sorting. These two factors may collectively explain the limited compositional variation observed among sandstones with different sizes.

Heavy Mineral Assemblage Aspect

The analysis revealed fluctuations in tourmaline abundance and GZI values (garnet abundance) between Clusters A and B, indicative of a different sedimentary provenance. Tourmaline, a weathering-resistant heavy mineral, is predominantly found in aluminum-enriched granites and its associated pegmatites, as well as in high-grade metamorphic rocks such as gneiss, amphibolite, and mica schist (Henry and Dutrow, 1996). This implies that the source rocks of samples in Clusters B are likely derived from Precambrian metamorphic complexes and Paleozoic and Triassic granitoids situated within the NK and SK regions (Fig. 1B), which is consistent with the results obtained from the observation of lithics (Fig. 4, 6–7). From a petrological perspective, we infer that the provenance of Cluster A samples is predominantly linked to mafic volcanic

eruptions. Nevertheless, garnet is generally not present in basaltic magmas, given its instability under the low-pressure crystallization conditions. Therefore, we advance the hypotheses that although the principal source is probably associated with mafic volcanic activity, there may also be contributions from other source regions. In particular, the widespread exposure of Triassic garnet-bearing Li–Be pegmatites and strongly peraluminous granites in the Muji–Bulunkou area (Fig. 1A), located southwest of the Qimgan and Oytag sections, along with their garnet-rich wall rocks (schists of the Bulunkuole Group), may have served as a potential source of detrital garnet (Yan et al., 2022). The concurrent occurrence of minor epidote with the ZTR fraction also implies that there may be additional contributions from other source regions (Glazer et al., 2023).

Detrital Zircon U-Pb Aspect

How Faithfully does the Modern River Signal Reflect the Jurassic Source Terranes?

As reported by previous publications, detrital zircon U-Pb age data were acquired from 11 modern river sand samples derived from the WKS and 16 samples sourced from the Pamir to delineate the geochronological signature of potential sediment provenances (Fig. 11; Lukens et al., 2012; Carrapa et al., 2014; Blayney et al., 2016; Liu et al., 2017). Throughout the Triassic–Jurassic, the CP and SP experienced extensive continental–marine transitional sedimentation (Fig. 1B; Rutte et al., 2017; Villarreal et al., 2020), and a Triassic–Jurassic basin is believed to have been situated between the NP and CP (Rembe et al., 2022), which was a consequence of the closure of the Paleo-Tethys Ocean (Schwab et al., 2004; Imrecke et al., 2019). This basin is likely analogous to the trough that accommodated a shallow sea, which spanned from the Band-e Bayan block in Afghanistan to the west (Girardeau et al., 1989) and Central Pamir to the eastern Tianshuihai terrane along the southern flanks of the WKS (Zhang et al., 2019b). This geological setup may have acted as a barrier to northward sediment transport from CP and SP during the Jurassic.

Furthermore, the detrital zircons from the CP and SP are distinguished by age peaks corresponding to the Cretaceous—Paleogene (Fig. 11; Lukens et al., 2012; Carrapa et al., 2014). Consequently, the results here align with the view of Zhang et al. (2019b), who propose that the WKS and NP constituted the principal source areas for the Jurassic sediments in the south-western Tarim Basin, with minimal contribution from the CP and SP.

In summary, the detrital zircon population from the WKS (n=1328) exhibits age group ranging from *ca* 950–600 Ma, 510–380 Ma, 260–180 Ma and 120–70 Ma (Fig. 11). Conversely, the NP displays a tightly clustered age distribution of detrital zircons (n=1058), predominantly between *ca* 230–190 Ma.Several lines of evidence were presented to support the fidelity of the modern river signal as a proxy for the Jurassic source terranes (WKS and NP). (1) The magmatism within the WKS and NP Terranes may be either entirely absent or significantly subdued following the Jurassic, suggesting minimal Cretaceous and Cenozoic impact on the Jurassic source signal. (2) The WKS–Pamir Paleo-Tethys Realm, particularly the NK–SK and NP Terranes, underwent significant thickening and uplift prior to the Jurassic due to the closure of the Paleo-Tethys Ocean (e.g., Bershaw et al., 2012; Villarreal et al., 2020), with post-collisional orogeny maintaining minimal source terrane changes. (3) Sobel (1999) posited that the Jurassic deposits in southwestern Tarim originated mainly from the Pamir's eastern margin and the westernmost Kunlun, resembling modern intermontane river systems in the south-western Tarim Basin. However, we acknowledge that the signal from modern river sands should be interpreted with care and may necessitate revision as additional data are acquired.

Spatial Differentiation of Detrital Zircon U-Pb Signals

The 3D-MDS clustering outcome (Fig. 13) exhibits a strong correspondence with the heavy mineral analysis (Fig. 8). The samples from the Qimgan section, Oytag section, and NP form a

relatively compact cluster (Group A). In contrast, a separate cluster is formed by the samples from the Toyunduk–Kyzyltau section, Fusha Region, and WKS (Group B).

638

639

640

641

642

643

644

645

646

647

648

649

650

651

652

653

654

655

656

657

658

659

660

A visual analysis of PDPs suggests that Group A is very similar to modern river sands derived from the NP (Fig. 12). The samples from both the Qimgan and Oytag sections are predominantly characterized by Triassic age populations, with those in the Oytag section also exhibiting age populations of Late Paleozoic (Fig. 12). Based on the current geological map and previous studies, two potential provenance domains in the NP are considered for the Jurassic sands: Late Paleozoic arc volcanic rocks and Triassic granitoid batholiths. The source of the Late Paleozoic detrital zircons is not in question and is generally attributed to bimodal volcanism induced by the northward subduction of the Paleo-Tethys along the north-eastern margin of the NP (e.g., Ji et al., 2017; Rembe et al., 2021; Song et al., 2024). These signatures are consistent with the igneous zircon ages (354–264 Ma) observed in the widely distributed volcanic rocks on the north-eastern margin of the Pamir Plateau (e.g., Zhang et al., 2006; Jiang et al., 2008; Rembe et al., 2021; Mu, 2016; Huangfu, 2018). As for the Triassic detrital zircons, existing hypotheses predominantly support a provenance from the granitoid batholiths that formed in response to the closure of the Paleo-Tethys Ocean and the subsequent continent-continent collision (Schwab et al., 2004; Imrecke et al., 2019; Zhang et al., 2019b). However, this interpretation is not fully consistent with the robust petrological evidence (the dominance of volcanogenic minerals, such as high-temperate quartz and basaltic lithics; Fig. 3) within the Qimgan-Oytag sandstones, which strongly suggests an volcanic provenance. The aforementioned evidence implies the potential existence of underreported Triassic aged volcanic sources within the NP.

Unsurprisingly, the provenance of Group B is inextricably linked to the rock units of the WKS.

Considering the geological map and prior research, the likely sediment sources for Group B

include the NK, SK, Tianshuihai, and Songpan—Ganzi Terranes (Fig. 1B). The PDPs of all samples within Group B exhibit identical dominant age modes, ranging from 850–750 Ma and 450–400 Ma, which correspond to the Precambrian metamorphic complex and the extensive Ordovician—Devonian granitoids exposed in the current NK and SK Terranes (e.g., Zhang et al., 2018; Yin et al., 2020). The absence of Triassic—Jurassic detrital zircons in the Fusha Region suggests that no fluvial system existed during the Jurassic that could have transported sediments across the intervening WKS—a prominent mountain range—linking the Tianshuihai and Songpan—Ganzi terranes to the Fusha Region. Samples KZLT1601 and KZLT1602, however, present a relatively complex age spectrum, including minor age populations of Late Paleozoic (Fig. 12G, H), indicating that there may have been additional provenance inputs alongside the primary NK–SK source. The proximal bimodal volcanism along the north-eastern margin of the NP were likely components of the mixed provenance for these two samples. Consequently, the proximal sources of the NK–SK were the principal contributors to the Jurassic sediments in Group B, with minor contributions from Late Paleozoic bimodal volcanic sources in the Toyunduk–Kyzyltau section.

Overall Provenance

Taken together, the Jurassic sediments exhibit clear characteristics of sedimentation from proximal sources. The sediments in Qimgan and Oytag are almost entirely sourced from nearby Triassic volcanic rocks, which may have been extensively eroded and are observed only in a few outcrops (Rembe et al., 2022). Although there is a potential contribution from the Triassic granitoid batholiths in the NP, they do not appear to represent the main source. The sub-populations of Late Paleozoic detrital zircons in Oytag and Toyunduk–Kyzyltau suggest sediment input from the bimodal volcanic sequence exposed along the north-eastern margin of the NP. The proximal sources of the NK–SK Terranes (Precambrian metamorphic complexes and Paleozoic granitoids)

were the principal contributors to the Early Paleozoic and Neoproterozoic sediments in Toyunduk– Kyzyltau and Fusha.

TECTONIC IMPLICATIONS

Some Remarks on the Significance of Triassic Volcanic Eruptions

The Triassic volcanic activity in the north-eastern Chinese Pamir has been the subject of only limited prior attention, in contrast to the more thoroughly documented Triassic volcanosedimentary sequences of the Afghanistan–Kyrgyzstan NP. Rembe et al. (2022) provided a detailed delineation of the Triassic volcanic activity within the Hindukush in Afghanistan and the northwestern Pamir regions in Tajikistan and Kyrgyzstan. Here, the key contents of their synthesis are summarized succinctly:

- 1 Along the north-western flank of the Hindukush in northern Afghanistan, felsic volcanic rocks ranging from Anisian to Latidian in age were observed (Wolfart and Wittekindt, 1980). Furthermore, the intercalation of lava flows (dated to the Norian using K-Ar radiometric dating) with terrigenous sandstones in the region, particularly in the Doab area of northern Afghanistan (Fig. 2A), attests to the extensive Triassic synsedimentary volcanism (Blaise et al., 1970). This setting is commonly interpreted as a back-arc basin, linked to the Paleo-Tethys subduction and volcanic arc activity (Siehl, 2015).
- 2 In the Altyn Darya valley of Kyrgyzstan NP (Fig. 2A), the prevalence of Rhaetian chemically immature volcanic clasts within a thick sequence of continental clastic deposits (*ca* 2500 meters) also signals a period of intense Triassic synsedimentary volcanism (Budanov, 1993). This volcanosedimentary succession is understood to be the product of a short-lived back-arc extensional basin (Salikhov and Sakiev, 2014).

Of greater significance, Rembe et al. (2022) reported outcrops of Triassic pyroclastic rocks ca 5 kilometers north-west of the Qimgan section, dated to 244.1 \pm 1.1 Ma, and a similar unit in the Gez valley (near the Oytag section) to 233.4 \pm 1.1 Ma. Bulk-rock geochemical analyses of these sequences suggest a volcanic back-arc origin. Therefore, in light of the aforementioned results, Rembe et al. (2022) posits that there may have been a more than 1000 kilometers long realm of Triassic back-arc extension to the north of the Paleo-Tethys subduction zone, extending across the north-eastern Chinese Pamir, the north-western flank of the Hindukush, the Doab area in northern Afghanistan, and the Altyn Darya valley of Kyrgyzstan NP.

In this study, the well-preserved Triassic volcanic lithics within the Jurassic deposits of the Qimgan–Oytag sections provide critical insights into the geodynamic crustal evolution of the NP (Fig. 3–5). The dated detrital zircons from the Qimgan–Oytag sections constrain the age of the volcanic lithics to between *ca* 250–210 Ma (Fig. 12A–F), aligning chronologically with the Triassic back-arc magmatism in the Altyn Darya valley of Kyrgyzstan NP and northern Afghanistan. This temporal correlation also coincides with the Karakul–Mazar granitoid batholiths on the NP, within the context of the Paleo-Tethys subduction (Schwab et al., 2004; Robinson et al., 2015). Therefore, considering the temporal and tectonic relationships, the Triassic volcanic activity near the Qimgan–Oytag sections may be also attributed to back-arc magmatism initiated by the closure of the Paleo-Tethys.

Based on the detrital zircon and petrological evidence presented in this study, we endorse the hypothesis posited by Rembe et al. (2022), suggesting that a NW-SE trending Triassic back-arc volcanic system was located in the north-eastern Chinese Pamir. This back-arc volcanic system likely extended southward from Oytag, ultimately ceasing its development at an unspecified location between Oytag and Toyunduk. Furthermore, these volcanic rocks served as the parent

rocks, providing detrital materials for the subsequent Jurassic deposits in the Qimgan and Oytag sections. This eruption event was kinematically linked to the back-arc formation associated with the Paleo-Tethys subduction along the southern Asian continental margin. Due to the significantly lower chemical stability of mafic volcanic rocks compared to granitoids, this may result in a relatively higher rate and intensity of erosion for these rocks. Thus, the lack of igneous rock outcrops from the current NP may be attributed to the intense and thorough denudation that occurred as a result of the India–Asia collision and the substantial uplift of the Pamir–Tibet Plateau during the Cenozoic (Hacker et al., 2017). However, it must be emphasized that further studies on tectonics and igneous processes are necessary to fully elucidate the geodynamic history of this Triassic volcanic eruption.

Jurassic tectono-sedimentary Patterns

Scholars have debated the precise timing of the WKS–Pamir Paleo-Tethys collisional orogeny, with proposals ranging from Late Permian–Middle Triassic (e.g., Jiang et al., 2013; Liu et al., 2015) to Late Triassic–Early Jurassic (e.g., Matte et al., 1996; Mattern and Schneider, 2000; Xiao et al., 2002; Wu et al., 2021). However, we align with the consensus that the orogeny, including crustal thickening and uplift, had concluded prior to the Jurassic. This intense orogenic activity caused significant deformation of pre-Jurassic strata, leading to the angular unconformity between Jurassic and Paleozoic systems (Wu et al., 2021), as illustrated in Figure 5B.

Figure 14 summarizes the interpreted Jurassic depositional model for the south-western Tarim Basin, though these are idealized types. Published isopach patterns indicate a Jurassic margin bounded by normal faults, parallel to the WKS–Pamir, which governed the sedimentation patterns and the variability in stratal thickness (e.g., Sobel, 1999; Wu, 2017). The initial stage, approximately corresponding to the J₁s and J₁k strata (Fig. 14A), is characterized by high sediment-

concentration floods that deposited proximal, coarse-grained alluvial fan-fan delta deposits (Figure 3B-C, 5B and 6B-C).

Sediment transport pathways were dominated by hillslope mass-wasting from the WKS (e.g., Toyunduk) and the NP (e.g., Qimgan–Oytag), conveyed through alluvial fan and intermontane river systems. Variations in potential provenance domains, pre-existing topography, and the extent of surface deformation influenced by normal faults resulted in significant petrological variability and spatial differentiation of detrital zircon U-Pb age distributions among individual outcrops/wells (Figs. 4 and 12). Subsequent lateral propagation between fault segments may have led to the expansion and coalescence of early fault depocenters (Gawthorpe and Leeder, 2000; Fig. 14B). Isolated lakes may have become largely interconnected at this stage. Extensive lake and swamp sedimentation were the dominant features during this stage (Figure 6D–E, J).

During the final stage, according to research by Wu et al. (2021, 2024), there may be areas where the J_1s – J_2t strata are in parallel unconformable contact with the J_3k strata induced by the northward subduction of the Neo-Tethys Ocean. The contractional event, governed by modifications in the subduction behavior of the Neo-Tethyan Oceanic crust from southward retreat to northward flat-slab advance, led to the uplift of the WKS–Pamir, profoundly influenced the tectonostratigraphic framework of the basin and altering the dynamics of its source-to-sink system. The death of the main border fault and ongoing sediment supply may have led to lacustrine accommodation becoming completely filled (approximately corresponding to the J_3k strata, Fig. 14C). The sedimentary signatures record the re-establishment of alluvial fan and fan-delta deposition sourced from the WKS and NP.

Possible Mechanisms of Jurassic Extension

The sedimentary facies in the study area exhibit a stratigraphic sequence from proximal alluvial fan to lacustrine deposits, terminating in coarse-grained alluvial-fan deposits (Fig. 14). The observed facies pattern conforms to that proposed for extensional basin models (Gawthorpe and Leeder, 2000) and aligns with Sobel's (1999) proposition of several narrow, deep, and separated extensional grabens developing along the WKS and NP during the Jurassic. Nevertheless, the diversity in detrital framework composition (Fig. 4), the distinct detrital zircon U-Pb age distributions (Fig. 12) and the basin scale suggest that the mechanisms governing extensional processes may exhibit variations.

The regional extension is primarily driven by back-arc extension, continental rifting linked to mantle plumes, and post-collisional extension from lithospheric thinning (Zheng and Dai, 2018). There is no evidence for the Mesozoic mantle plumes recorded in or around the Tarim Basin. The Jurassic setting of the Qimgan and Oytag sections likely inherited the Triassic back-arc extension, with the basin orientation adopting a NW-SE trend, aligned parallel to the WKS-Pamir axis. Evidence for this includes: 1) The zircon age populations exhibit a restricted distribution, with major peak ages closely approximate the timing of sediment accumulation (Fig. 12). These spatial and temporal variations in sediment provenance are most plausibly explained by basins located along plate margins with synsedimentary magmatic activity (Cawood et al., 2012), which aligns with the tectonic interpretations in the Triassic. 2) The sandstones are predominantly composed of mafic volcaniclastic debris and high-temperate quartz (Fig. 3–5), indicating a significant contribution of Triassic back-arc eruption to the supply of Jurassic sediments.

In contrast, the Jurassic Toyunduk–Kyzyltau and Fusha are more likely to be interpreted as a rift basin that formed in the outcome of post-collisional extension, which was triggered by isostatic rebound. Evidence for this includes: 1) The Toyunduk–Kyzyltau and Fusha region are

distinguished by detrital zircon ages that significantly predate the depositional age (Fig. 12), indicating that the sediment supply was largely influenced by the stable presence of the provenance area, rather than by syn-sedimentary volcanic activity. 2) The sandstones, primarily composed of quartz with rough grain surfaces and high-grade metamorphic lithics (Fig. 4, 6–7), similarly suggest a provenance that may have been relatively stable at a tectonic scale. 3) A growing body of evidence suggests that the cooling event, significant crustal thickening and the associated extensive surface uplift occurred across the WKS during the Late Permian–Triassic (e.g., Matte et al., 1996; Kapp et al., 2007; Cao et al., 2015; Li et al., 2019a). This event may mark a stage in the region's tectonic evolution, where the typical sequence of orogenic belt development in collisional settings—characterized by crustal thickening, surface uplift, a period of tectonic quiescence, isostatic rebound, and culminating in extensional collapse (Wolf et al., 2022)—was initiated.

Moreover, previous study of extensional basins in the southwestern Tarim region has revealed a structural configuration that is in accordance with the geometric and kinematic characteristics during the Mesozoic in the central Asia (Sobel, 1999). The NW–SE orientation—extending from Qimgan to Toyunduk—was broadly consistent with the regional stress field associated with the Talas-Ferghana Fault (TFF), a major NNW-striking dextral strike-slip fault system active since the Mesozoic (Fig. 2A). Although the TFF is not the primary focus of this study, its role in shaping the regional stress regime during the Jurassic cannot be overlooked. These trends reflect the structural weaknesses that localized deformation and directed the development of the basin. Therefore, the Qimgan–Toyunduk Jurassic Basin developed within an extensional regime that was closely related to the regional stress field governing the TFF. This result highlights the interplay between local fault development and tectonic processes.

Geodynamic Model

Carboniferous-Triassic Pre-collision Phase

The NP displays a characteristic northward-convex structural configuration (Li et al., 2020). Since the Carboniferous, the northward subduction of the Paleo-Tethys Ocean initiated the development of an arc system and facilitated the early evolution of a back-arc basin (Fig. 15A). Notably, in the southwestern Oytag Section, this tectonic regime promoted the formation of a Carboniferous—Permian back-arc basin, accompanied by the emplacement of bimodal volcanic rocks (Song et al., 2024). These volcanic sequences played a crucial role in supplying detrital material of the overlying Jurassic sedimentary succession in the Oytag Section.

Triassic Syn-collision Phase

From a provenance perspective, the south-western Tarim Basin can be divided into two domains: the Paleo-Tethys–NP, influencing the Qimgan to Oytag sections, and the Paleo-Tethys–WKS, governing the Toyunduk–Kyzyltau section to Fusha region (Fig. 15B). For the former, the closure of Paleo-Tethys Ocean led to the collision between the Qiangtang Terrane and the SK Terrane, causing intense uplifting and denudation of south-western Tarim Basin (Zheng et al., 2015; Xu et al., 2020). The scarcity of Triassic sediments is attributed to the northward tilting and uplift of the terrain (e.g., McFadden et al., 1988; Zhu et al., 2013). In contrast, the Paleo-Tethys–NP domain was characterized by an extensional back-arc zone and calc-alkaline magmatic activity, initiated by the northward subduction of the Paleo-Tethys Ocean. This activity extended approximately one thousand kilometers along the northern margin of the NP (Blaise et al., 1970; Siehl, 2015; Rembe et al., 2022; Li et al., 2022), bridging the Doab area to the west with the Qimgan–Oytag area to the east. Shortly thereafter, a *ca* 100-kilometer-wide collision-related granitoid belt, ranging from 243–210 Ma (Wei, 2018), formed in the Karakul–Mazar–Songpan–

Ganzi region (Schwab et al., 2004; Robinson et al., 2015), indicating the final closure of the Paleo-Tethys Ocean.

Jurassic Post-collisional Extension Phase

The basal Jurassic proximal alluvial fan deposits serve as a geological record of the waning stages of collisional orogeny, indicating that the closure of the Paleo-Tethys Ocean and the resultant primary collision event had largely concluded prior to the Jurassic (e.g., Imrecke et al., 2019; Villarreal et al., 2020). Concurrently, the NP and NK–SK Terranes experienced pronounced uplift as a consequence of the collisional orogeny, effectively separating the distant sediment provenance of the Tianshuihai/Songpan–Ganzi/CP–SP Terranes either progressively or entirely. During this time, several narrow, deep, and separated post-collisional extensional grabens developed parallel to the south-western margin of the WKS and NP. In particular, the structural configuration and NW–SE orientation of Jurassic extensional basins from Qimgan to Toyunduk align with the regional stress field governed by the TTF, underscoring the influence of inherited tectonic structures on basin development (Fig. 15C). Overall, the Jurassic sedimentary record is predominantly sourced from nearby back-arc igneous rocks or recycled orogen. There is also a partial contribution from the Triassic granitoid batholiths in the NP. These rocks were transported by hillslope mass wasting via alluvial fan and intermontane river systems.

CONCLUSIONS

- Integration of new sedimentological, petrological, and geochronological data with published datasets on the Jurassic strata from the Tarim Basin, present the following conclusions.
- (1) In terms of provenance analysis, the south-western Tarim can be delineated into two tectonic domains: the Paleo-Tethys-NP (Qimgan, Oytag) and the Paleo-Tethys-WKS (Toyunduk-

Kyzyltau and Fusha). For the former, Jurassic clastic rocks are inferred to have been predominantly sourced from the NP, specifically from Triassic and Late Paleozoic arc-related volcanic sequences, with minor contribution from the Triassic granitoid batholiths In contrast, the Jurassic deposits in the Paleo-Tethys–WKS domain are thought to have been largely derived from the NK–SK Terranes, which include Early Paleozoic collisional granitoid batholiths and Proterozoic metamorphic crystalline basement.

- (2) The well-preserved Triassic volcanic lithics within the Jurassic deposits of the Qimgan—Oytag sections are indicative of a Triassic back-arc volcanic event linked to the Paleo-Tethys subduction, supporting the hypothesis of such activity in the north-eastern Chinese Pamir. These volcanic rocks served as the principal source of the Jurassic deposits.
- (3) The Jurassic rifting observed in the Qimgan–Oytag region may be attributed to the tectonic inheritance of Triassic back-arc extension, while from the perspective of the driving mechanism of regional extension, the rifting in the Toyunduk–Kyzyltau and Fusha regions is more likely interpreted as post-collisional extension driven by isostatic rebound.

ACKNOWLEDGMENTS

The research presented was funded by the National Natural Science Foundation of China under Grant No. 42272109. We extend our gratitude to the Research Institute of Petroleum Exploration and Development, Tarim Oilfield Company, PetroChina (Korla), for granting us access to the industrial data that were instrumental in our research endeavors. We appreciate the insightful comments and constructive feedback provided by the Science Editor, Professor Mihai Ducea, and the Associate Editor, Professor Rajat Mazumder, which have undoubtedly contributed to the refinement and enhancement of our manuscript. Additionally, we wish to acknowledge the

Professors Heinrich Bahlburg, Edward Sobel and one anonymous reviewer for their meticulous reviews and valuable suggestions, which have played a pivotal role in strengthening the quality of this work. Lastly, we extend our gratitude to Dr. Ke Yang and Dr. Yichao Li for their invaluable assistance with the data processing associated with the detrital zircon U-Pb geochronology experiment, as well as to Dr. Langtao Liu from the Hebei University of Engineering for his provision of the detrital zircon data that was integral to this study.

895

896

909

Ferrand.

889

890

891

892

893

894

REFERENCES CITED

897 Aminov, J., Ding, L., Mamadjonov, Y., Dupont-Nivet, G., Aminov, J., Zhang, L.Y., Yoqubov, S., 898 Aminov, J., and Abdulov, S., 2017, Pamir Plateau formation and crustal thickening before 899 the India–Asia collision inferred from dating and petrology of the 110–92 Ma Southern Pamir 900 volcanic sequence: Gondwana Research, v. 51, p. 310–326, doi: 10.1016/j.gr.2017.08.003. 901 Aminov, J., Roperch, P., Dupont-Nivet, G., Cordier, C., Guillot, S., Glodny, J., Timmerman, M.J., 902 Sudo, M., Ruffet, G., Wilke, M., Lagroix, F., Lin, D., and Mamadjanov, Y., 2023, 903 Contractional deformation between extensional dome exhumation in Central Pamir at 17-904 15 Ma constrained by metamorphic and paleomagnetic data from the Bartang volcanic rocks, 905 Tajikistan: Tectonophysics, v. 868, p. 230080, doi: 10.1016/j.tecto.2023.230080. Arnaud, N.O., 1992, Apport de la thermochronologie ⁴⁰Ar/³⁹Ar sur feldspath potassique à la 906 907 connaissance de la tectonique Cenozoique d'Asie: étude des mécanismes d'accomodation de 908 la collision continentale [Ph.D. thesis]: Clermont-Ferrand, France, University of Clermont-

- Bazhenov, M.L., 1996, Permo-Triassic paleomagnetism of the North Pamir: tectonic implications:
- 911 Earth and Planetary Science Letters, v. 142, p. 109–120, doi: 10.1016/0012-821x(96)00090-
- 912 8.
- 913 Bershaw, J., Garzione, C.N., Schoenbohm, L., Gehrels, G., and Tao, L., 2012, Cenozoic evolution
- of the Pamir Plateau based on stratigraphy, zircon provenance, and stable isotopes of foreland
- basin sediments at Oytag (Wuyitake) in the Tarim Basin (west China): Journal of Asian Earth
- 916 Sciences, v. 44, p. 136–148, doi: 10.1016/j.jseaes.2011.04.020.
- 917 Blaise, J., Bordet, P., Lang, J., De, L.A.F., Leutwein, F., Sonet, J., 1970, Mesures
- 918 géochronologiques de quelques roches cristallines d'Afghanistan central, Comptes Rendus,
- 919 Académie des Sciences, v. 270, p. 2772–2775.
- 920 Blayney, T., Najman, Y., Dupont-Nivet, G., Carter, A., Millar, I., Garzanti, E., Sobel, E.R., Rittner,
- 921 M., Andò, S., Guo, Z., and Vezzoli, G., 2016, Indentation of the Pamirs with respect to the
- northern margin of Tibet: Constraints from the Tarim Basin sedimentary record: Tectonics,
- 923 v. 35, p. 2345–2369, doi: 10.1002/2016tc004222.
- Bohor, B.F., and Triplehorn, D.M., 1993, Tonsteins: Altered volcanic-ash layers in coal-bearing
- 925 sequences: 285: Tonsteins: Altered Volcanic-Ash Layers in Coal-Bearing Sequences, p. 1–
- 926 44, doi: 10.1130/spe285-p1.
- 927 Budanov, V.I, 1993, Endogenous Formations of the Pamirs, Donish, Dushanbe.
- 928 Burtman, V.S., and Molnar, P., 1993, Geological and geophysical evidence for deep subduction
- of continental crust beneath the Pamir: Geological Society of America Special Papers, p. 1–
- 930 76, doi: 10.1130/spe281-p1.
- Cao, K., Wang, G.C., Bernet, M., van der Beek, P., and Zhang, K.X., 2015, Exhumation history
- of the West Kunlun Mountains, northwestern Tibet: Evidence for a long-lived, rejuvenated

- orogen: Earth and Planetary Science Letters, v. 432, p. 391-403, doi:
- 934 10.1016/j.eps1.2015.10.033.
- Carrapa, B., Mustapha, F.S., Cosca, M., Gehrels, G., Schoenbohm, L.M., Sobel, E.R., DeCelles,
- P.G., Russell, J., and Goodman, P., 2014, Multisystem dating of modern river detritus from
- 937 Tajikistan and China: Implications for crustal evolution and exhumation of the Pamir:
- 938 Lithosphere, v. 6, p. 443–455, doi: 10.1130/l360.1.
- 939 Castillo, P., Bahlburg, H., Fernandez, R., Fanning, C.M., and Berndt, J., 2022, The European
- ontinental crust through detrital zircons from modern rivers: Testing representativity of
- detrital zircon U-Pb geochronology: Earth-Science Reviews, v. 232, p. 104145, doi:
- 942 10.1016/j.earscirev.2022.104145.
- 943 Cawood, P.A., Hawkesworth, C.J., and Dhuime, B., 2012, Detrital zircon record and tectonic
- 944 setting: Geology, v. 40, p. 875–878, doi: 10.1130/g32945.1.
- Chapman, J.B., Carrapa, B., Ballato, P., DeCelles, P.G., Worthington, J., Oimahmadov, I., Gadoev,
- M., and Ketcham, R., 2017, Intracontinental subduction beneath the Pamir Mountains:
- 947 Constraints from thermokinematic modeling of shortening in the Tajik fold-and-thrust belt:
- 948 GSA Bulletin, doi: 10.1130/b31730.1.
- Chapman, J.B., Robinson, A.C., Carrapa, B., Villarreal, D., Worthington, J., DeCelles, P.G., Kapp,
- P., Gadoev, M., Oimahmadov, I., and Gehrels, G., 2018a, Cretaceous shortening and
- exhumation history of the South Pamir terrane: Lithosphere, v. 10, p. 494–511, doi:
- 952 10.1130/1691.1.
- 953 Chapman, J.B., Scoggin, S.H., Kapp, P., Carrapa, B., Ducea, M.N., Worthington, J., Oimahmadov,
- I., and Gadoev, M., 2018b, Mesozoic to Cenozoic magmatic history of the Pamir: Earth and
- 955 Planetary Science Letters, v. 482, p. 181–192, doi: 10.1016/j.epsl.2017.10.041.

- 956 Corfu, F., 2003, Atlas of zircon textures: Reviews in Mineralogy and Geochemistry, v. 53, p. 469–
- 957 500, doi: 10.2113/0530469.
- 958 Cowgill, E., 2009, Cenozoic right-slip faulting along the eastern margin of the Pamir Salient,
- Northwestern China: Geological Society of America Bulletin, v. 122, p. 145–161, doi:
- 960 10.1130/b26520.1.
- 961 Cowgill, E., Yin, A., Harrison, T.M., and Wang X.F., 2003, Reconstruction of the Altyn Tagh
- Fault based on U-Pb geochronology: Role of back thrusts, mantle sutures, and heterogeneous
- crustal strength in forming the Tibetan Plateau: Journal of Geophysical Research: Solid Earth,
- 964 v. 108, doi: 10.1029/2002jb002080.
- 965 Ding, L., Yang, D., Cai, F.L., Pullen, A., Kapp, P., Gehrels, G.E., Zhang, L.Y., Zhang, Q.H., Lai,
- 966 Q.Z., Yue, Y.H., and Shi, R.D., 2013, Provenance analysis of the Mesozoic Hoh-Xil-
- Songpan-Ganzi turbidites in northern Tibet: Implications for the tectonic evolution of the
- eastern Paleo-Tethys Ocean: Tectonics, v. 32, p. 34–48, doi: 10.1002/tect.20013.
- 969 Faisal, S., Larson, K.P., King, J., and Cottle, J.M., 2016, Rifting, subduction and collisional records
- 970 from pluton petrogenesis and geochronology in the Hindu Kush, NW Pakistan: Gondwana
- 971 Research, v. 35, p. 286–304, doi: 10.1016/j.gr.2015.05.014.
- 972 Fang, W.X., Wang, L., Guo, Y.Q., Li, T.C. Jia, R.X., and Liu, Z.R., 2018, Tectonic patterns in the
- Sarekebayi apart-pull basin and their ore-controlling regularities for the Sareke glutenite-type
- opper deposit in Xinjiang, China: Earth Science Frontiers, v. 25, p. 240–259, doi:
- 975 10.13745/j.esf.yx.2017-12-20.
- 976 Folk, R.L.,1980, Petrology of Sedimentary Rocks. Hemphill Publ. Co., Austin, 185 pp.
- 977 Garzanti, E., 2019, Petrographic classification of sand and sandstone: Earth-Science Reviews, v.
- 978 192, p. 545–563, doi: 10.1016/j.earscirev.2018.12.014.

- 979 Garzanti, E., Resentini, A., Vezzoli, G., Andò, S., Malusà, M.G., Padoan, M., and Paparella, P.,
- 980 2010, Detrital fingerprints of fossil continental-subduction zones (axial belt provenance,
- 981 European Alps): The Journal of Geology, v. 118, p. 341–362, doi: 10.1086/652720.
- 982 Galloway, W.E., 1974, Deposition and diagenetic alteration of sandstone in northeast Pacific Arc-
- 983 related basins: Implications for graywacke genesis: Geological Society of America Bulletin,
- 984 v. 85, p. 379, doi: 10.1130/0016-7606(1974)85<379:dadaos>2.0.co;2.
- 985 Gawthorpe, R.L., and Leeder, M.R., 2000, Tectono-sedimentary evolution of active extensional
- 986 basins: Basin Research, v. 12, p. 195–218, doi: 10.1046/j.1365-2117.2000.00121.x.
- 987 Gibbons, A.D., Zahirovic, S., Müller, R.D., Whittaker, J.M., and Yatheesh, V., 2015, A tectonic
- 988 model reconciling evidence for the collisions between India, Eurasia and intra-oceanic arcs
- of the central-eastern Tethys: Gondwana Research, v. 28, p. 451-492, doi:
- 990 10.1016/j.gr.2015.01.001.
- 991 Glazer, A., Avigad, D., Morag, N., and Gerdes, A., 2023, Tracing Oligocene-Miocene source-to-
- sink systems in the Deep Levant Basin: A sandstone provenance study: Geological Society
- 993 of America Bulletin, v. 136, p. 1587–1604, doi: 10.1130/b36864.1.
- 994 Girardeau, J., Marcoux, J., and Montenat, C., 1989, The Neo-Cimmerian Ophiolite Belt in
- Afghanistan and Tibet: Comparison and Evolution. Tectonic Evolution of the Tethyan
- 996 Region. Springer, p. 477–504.
- 997 Golonka, J., and Bocharova, N.Y., 2000, Hot spot activity and the break-up of Pangea:
- Palaeogeography, Palaeoclimatology, Palaeoecology, v. 161, p. 49–69, doi: 10.1016/s0031-
- 999 0182(00)00117-6.
- 1000 Graham, S.A., Hendrix, M.S., Wang, L.B., and Carroll, A.R., 1993, Collisional successor basins
- of western China: Impact of tectonic inheritance on sand composition: Geological Society of

- 1002 America Bulletin, v. 105, p. 323-344, doi: 10.1130/0016-
- 1003 7606(1993)105<0323:csbowc>2.3.co;2.
- 1004 Grant, M.L., Wilde, S.A., Wu, F., and Yang, J., 2009, The application of zircon
- cathodoluminescence imaging, Th-U-Pb chemistry and U-Pb ages in interpreting discrete
- magmatic and high-grade metamorphic events in the North China Craton at the
- 1007 Archean/Proterozoic boundary: Chemical Geology, v. 261, p. 155-171, doi
- 1008 10.1016/j.chemgeo.2008.11.002.
- Hacker, B.R., Ratschbacher, L., Rutte, D., Stearns, M.A., Malz, N., Stübner, K., Kylander-Clark,
- 1010 A.R., Pfänder, J.A., and Everson, A., 2017, Building the Pamir-Tibet Plateau—Crustal
- stacking, extensional collapse, and lateral extrusion in the Pamir: 3. Thermobarometry and
- petrochronology of deep Asian crust: Tectonics, v. 36, p. 1743–1766, doi:
- 1013 10.1002/2017tc004488.
- Hendrix, M.S., Graham, S.A., Carroll, A.R., Sobel, E.R., McKnight, C.L., Schulein, B.J., and
- Wang, Z.X., 1992, Sedimentary record and climatic implications of recurrent deformation in
- the Tian Shan: Evidence from Mesozoic strata of the north Tarim, south Junggar, and Turpan
- Basins, northwest China: Geological Society of America Bulletin, v. 104, p. 53–79, doi:
- 10.1130/0016-7606(1992)104<0053:sracio>2.3.co;2.
- Henry, D.J., and Dutrow, B.L., 1996, Chapter 10. Metamorphic tourmaline and its petrologic
- applications: Boron, p. 503–558, doi: 10.1515/9781501509223-012.
- Huangfu, X.K., 2018, Geochemical characteristics and metallogenic mechanism of copper
- polymetallic deposit in Kungaishan mountain [M.S. thesis]: Beijing, China, China University
- of Geosciences.

- Hubert, J.F., 1962. A zircon-tourmaline-rutile maturity index and the interdependence of the
- 1025 composition of heavy mineral assemblages with the gross composition and texture of
- sandstones. Journal of Sedimentary Research, v. 32, p. 440–450, doi: 10.1306/74d70ce5-
- 1027 2b21-11d7-8648000102c1865d.
- 1028 Ji, W.H., Chen, S.J., Li, R.S., He, S.P., Zhao, Z.M., and Pan, X.P., 2017, The origin of
- 1029 Carboniferous-Permian magmatic rocks in Oytag area, West Kunlun: Back-arc basin?. Acta
- 1030 Petrologica Sinica, v. 34, p. 2393–2409.
- Jiang, Y.H., Jia, R.Y., Liu, Z., Liao, S.Y., Zhao, P., and Zhou, Q., 2013, Origin of middle Triassic
- high-K calc-alkaline granitoids and their potassic microgranular enclaves from the western
- Kunlun Orogen, Northwest China: A record of the closure of Paleo-Tethys: Lithos, v. 156–
- 1034 159, p. 13–30, doi: 10.1016/j.lithos.2012.10.004.
- Jiang, Y.H., Liao, S.Y., Yang, W.Z., and Shen, W.Z., 2008, An island arc origin of plagiogranites
- at Oytag, western Kunlun orogen, northwest China: SHRIMP zircon U–Pb chronology,
- elemental and Sr–Nd–Hf isotopic geochemistry and Paleozoic tectonic implications: Lithos,
- 1038 v. 106, p. 323–335, doi: 10.1016/j.lithos.2008.08.004.
- Johnsson, M.J., 1993, The system controlling the composition of clastic sediments, in Johnsson,
- 1040 M.J. and Basu, A. eds., Processes Controlling the Composition of Clastic Sediments
- Geological Society of America, Special Paper 284, p. 1–19.
- 1042 Imrecke, D.B., Robinson, A.C., Owen, L.A., Chen, J., Schoenbohm, L.M., Hedrick, K.A., Lapen,
- T.J., Li, W.Q., and Yuan, Z.D., 2019, Mesozoic evolution of the eastern Pamir: Lithosphere,
- v. 11, p. 560–580, doi: 10.1130/11017.1.
- Ji, W.Q., Wu, F.Y., Wang, J.M., Liu, X.C., Liu, Z.C., Zhang, Z., Cao, W., Wang, J.G., and Zhang,
- 1046 C., 2020, Early evolution of Himalayan Orogenic Belt and generation of Middle Eocene

- magmatism: Constraint from Haweng Granodiorite Porphyry in the Tethyan Himalaya:
- 1048 Frontiers in Earth Science, v. 8, doi: 10.3389/feart.2020.00236.
- Kapp, P., DeCelles, P.G., Gehrels, G.E., Heizler, M., and Ding, L., 2007, Geological Records of
- the Lhasa-Qiangtang and Indo-Asian collisions in the Nima area of Central Tibet: Geological
- Society of America Bulletin, v. 119, p. 917–933, doi: 10.1130/b26033.1.
- 1052 Kellett, D.A., and Grujic, D., 2012, New insight into the South Tibetan detachment system: Not a
- single progressive deformation: Tectonics, v. 31, doi: 10.1029/2011tc002957.
- Li, G., Sandiford, M., Fang, A., Kohn, B., Sandiford, D., Fu, B., Zhang, T., Cao, Y., and Chen, F.,
- 2019a, Multi-stage exhumation history of the West Kunlun orogen and the amalgamation of
- the Tibetan Plateau: Earth and Planetary Science Letters, v. 528, p. 115833, doi:
- 1057 10.1016/j.epsl.2019.115833.
- Li, T.F., and Zhang, J.X., 2014, Zircon LA-ICPMS U-Pb ages of websterite and basalt in Kudi
- ophiolite and the implications, West Kunlun: Acta Petrologica Sinica, v. 30, p. 2393–2401.
- Li, T., Chen, Z., Chen, J., Thompson Jobe, J.A., Burbank, D.W., Li, Z., He, X., Zheng, W., Zhang,
- P., and Zhang, B., 2019b, Along-strike and downdip segmentation of the Pamir frontal thrust
- and its association with the 1985 M_w6.9 Wuqia earthquake: Journal of Geophysical Research:
- Solid Earth, v. 124, p. 9890–9919, doi: 10.1029/2019jb017319.
- Li, Y., Robinson, A.C., Zucali, M., Gadoev, M., Oimuhammadzoda, I., Lapen, T.J., and Carrapa,
- B., 2022, Mesozoic tectonic evolution in the Kurgovat-Vanch Complex, NW Pamir:
- Tectonics, v. 41, doi: 10.1029/2021tc007180.
- Li, Y.P., Robinson, A.C., Gadoev, M., and Oimuhammadzoda, I., 2020, Was the Pamir salient
- built along a Late Paleozoic embayment on the southern Asian margin? Earth and Planetary
- Science Letters, v. 550, p. 116554, doi: 10.1016/j.epsl.2020.116554.

- 1070 Liati, A., Gebauer, D., and Wysoczanski, R., 2002, U-Pb SHRIMP-dating of zircon domains from
- 1071 UHP garnet-rich mafic rocks and late pegmatoids in the Rhodope zone (N Greece); evidence
- for Early Cretaceous crystallization and Late Cretaceous metamorphism: Chemical Geology,
- v. 184, p. 281–299, doi: 10.1016/s0009-2541(01)00367-9.
- 1074 Linnemann, U., Ouzegane, K., Drareni, A., Hofmann, M., Becker, S., Gärtner, A., and Sagawe,
- 1075 A., 2011, Sands of West Gondwana: An archive of secular magmatism and plate
- interactions—A case study from the Cambro-Ordovician section of the Tassili Ouan Ahaggar
- 1077 (Algerian Sahara) using U-Pb-LA-ICP-MS detrital zircon ages: Lithos, v. 123, p. 188-203,
- 1078 doi: 10.1016/j.lithos.2011.01.010.
- Liu, L.T., Chen, J., and Li, T., 2017, Detrital zircon U-Pb dating of modern rivers' deposits in
- Pamir, South Tian Shan and their convergence zone: Seismology and Geology, v. 39, p. 497–
- 1081 516, doi: 10.3969/j.issn.0253-4967.2017.03.005.
- 1082 Liu, X.Q., Zhang, C.L., Zou, H., Wang, Q., Hao, X.S., Zhao, H.X., and Ye, X.T., 2020, Triassic-
- Jurassic granitoids and pegmatites from western Kunlun-Pamir Syntax: Implications for the
- paleo-Tethys evolution at the northern margin of the Tibetan Plateau: Lithosphere, v. 2020,
- 1085 doi: 10.2113/2020/7282037.
- Liu, X.Q., Zhang, C.L., Zou, H., and Ye, X.T., 2023, Diverse metavolcanic sequences in the
- 1087 Cambrian accretionary complex at the Pamir Syntax: Implications for tectonic evolution from
- Proto-Tethys to Paleo-Tethys: Journal of Asian Earth Sciences, v. 241, p. 105481, doi:
- 10.1016/j.jseaes.2022.105481.
- Liu, Z., Jiang, Y.H., Jia, R.Y., Zhao, P., and Zhou, Q., 2015, Origin of late Triassic high-k calc-
- alkaline granitoids and their potassic microgranular enclaves from the western Tibet Plateau,

- Northwest China: Implications for paleo-Tethys evolution: Gondwana Research, v. 27, p.
- 1093 326–341, doi: 10.1016/j.gr.2013.09.022.
- Liu, Z.S., 2022, Jurassic palynofloral Provinces of Tarim Basin: Journal of Stratigraphy, v. 26 p.
- 1095 18–26.
- Luo, H., Xiong, F., Huang, H., Yan, D., Zhang, D., Li, F., and Hou, M., 2024, Provenance of late
- 1097 Carboniferous–Triassic clastic rocks in the Western Kunlun orogenic belt, western China:
- Implications for the tectonic evolution of the Paleo-Tethys Ocean: Journal of Asian Earth
- 1099 Sciences, v. 267, p. 106162, doi: 10.1016/j.jseaes.2024.106162.
- Lukens, C.E., Carrapa, B., Singer, B.S., and Gehrels, G., 2012, Miocene exhumation of the Pamir
- revealed by detrital geothermochronology of Tajik rivers: Tectonics, v. 31, doi:
- 1102 10.1029/2011tc003040.
- 1103 Matte, P., Tapponnier, P., Arnaud, N., Bourjot, L., Avouac, J.P., Vidal, Ph., Liu, Q., Pan, Y.S.,
- and Wang, Y., 1996, Tectonics of Western Tibet, between the Tarim and the Indus: Earth and
- Planetary Science Letters, v. 142, p. 311–330, doi: 10.1016/0012-821x(96)00086-6.
- 1106 Mattern, F., and Schneider, W., 2000, Suturing of the Proto- and Paleo-Tethys oceans in the
- western Kunlun (Xinjiang, China): Journal of Asian Earth Sciences, v. 18, p. 637–650, doi:
- 1108 10.1016/s1367-9120(00)00011-0.
- 1109 McFadden, P.L., Ma, X.H., McElhinny, M.W., and Zhang, Z.K., 1988, Permo-Triassic
- magnetostratigraphy in China: northern Tarim: Earth and Planetary Science Letters, v. 87, p.
- 1111 152–160, doi: 10.1016/0012-821x(88)90071-4.
- Metcalfe, I., 2021, Multiple Tethyan ocean basins and orogenic belts in Asia: Gondwana Research,
- v. 100, p. 87–130, doi: 10.1016/j.gr.2021.01.012.

- Morton, A.C., and Hallsworth, C., 1994, Identifying provenance-specific features of detrital heavy
- mineral assemblages in sandstones: Sedimentary Geology, v. 90, p. 241-256, doi:
- 1116 10.1016/0037-0738(94)90041-8.
- 1117 Mu, S.L., 2016, Volcanic rocks tectonic environments and metallogenesis of typical mineral
- deposits in Kungai Mountains, West Kunlun [Ph.D. thesis]: Guangzhou, China, University
- of Chinese Academy of Sciences.
- Omodeo-Salé, S., Deschamps, R., Michel, P., Chauveau, B., and Suárez-Ruiz, I., 2017, The coal-
- bearing strata of the Lower Cretaceous Mannville Group (Western Canadian Sedimentary
- Basin, South Central Alberta), part 2: Factors controlling the composition of organic matter
- accumulations: International Journal of Coal Geology, v. 179, p. 219–241, doi:
- 1124 10.1016/j.coal.2017.05.020.
- Panca, F., Bahlburg, H., Cárdenas, J., Berndt, J., Lünsdorf, N.K., and Gerdes, A., 2024,
- Sedimentology, geochronology and provenance of the late permian and Triassic Mitu Group
- in Peru—The evolution of continental facies along a transform margin: Basin Research, v.
- 36, doi: 10.1111/bre.12864.Paton, C., Woodhead, J.D., Hellstrom, J.C., Hergt, J.M., Greig,
- A., and Maas, R., 2010, Improved Laser Ablation U–Pb zircon geochronology through robust
- downhole fractionation correction: Geochemistry, Geophysics, Geosystems, v. 11, doi:
- 1131 10.1029/2009gc002618.
- Pittman, E.D., 1970, Plagioclase feldspar as an indicator of provenance in sedimentary rocks:
- Journal of Sedimentary Research, v. 40, p. 591–598, doi: 10.1306/74d71fdc-2b21-11d7-
- 1134 8648000102c1865d.
- Rembe, J., Sobel, E.R., Kley, J., Terbishalieva, B., Musiol, A., Chen, J., and Zhou, R., 2022,
- Geochronology, geochemistry, and geodynamic implications of Permo-Triassic back-arc

- basin successions in the North Pamir, Central Asia: Lithosphere, v. 2022, doi:
- 1138 10.2113/2022/7514691.
- Rembe, J., Sobel, E.R., Kley, J., Zhou, R., Thiede, R., and Chen, J., 2021, The carboniferous arc
- of the North Pamir: Lithosphere, v. 2021, doi: 10.2113/2021/6697858.
- Rittner, M., Vermeesch, P., Carter, A., Bird, A., Stevens, T., Garzanti, E., Andò, S., Vezzoli, G.,
- Dutt, R., Xu, Z., and Lu, H., 2016, The provenance of Taklamakan Desert Sand: Earth and
- Planetary Science Letters, v. 437, p. 127–137, doi: 10.1016/j.epsl.2015.12.036.
- Robinson, A.C., Yin, A., Manning, C.E., Harrison, T.M., Zhang, S. H., and Wang, X.F., 2004,
- Tectonic evolution of the northeastern Pamir: Constraints from the northern portion of the
- 1146 Cenozoic Kongur Shan extensional system, western China: Geological Society of America
- Bulletin, v. 116, p. 953, doi: 10.1130/b25375.1.
- Robinson, A.C., Yin, A., Manning, C.E., Harrison, T.M., Zhang, S.H., and Wang, X.F., 2007,
- 1149 Cenozoic evolution of the eastern pamir: Implications for strain-accommodation mechanisms
- at the western end of the Himalayan-tibetan orogen: Geological Society of America Bulletin,
- v. 119, p. 882–896, doi: 10.1130/b25981.1.
- Robinson, A.C., 2015, Mesozoic tectonics of the Gondwanan terranes of the Pamir plateau: Journal
- of Asian Earth Sciences, v. 102, p. 170–179, doi: 10.1016/j.jseaes.2014.09.012.
- Rutte, D., Ratschbacher, L., Schneider, S., Stübner, K., Stearns, M.A., Gulzar, M.A., and Hacker,
- B.R., 2017, Building the Pamir-Tibetan Plateau—Crustal stacking, extensional collapse, and
- lateral extrusion in the Central Pamir: 1. Geometry and kinematics: Tectonics, v. 36, p. 342–
- 384, doi: 10.1002/2016tc004293.

- Salikhov, F.S., and Sakiev, K.S., 2014, Stages of sedimentation in the Permian-Triassic North
- Pamirs: Bulletin of the Institute of the National Academy of Sciences of the Kyrgyz Republic,
- 1160 v. 4.
- Saylor, J.E., and Sundell, K.E., 2016, Quantifying comparison of large detrital geochronology data
- sets: Geosphere, v. 12, p. 203–220, doi: 10.1130/ges01237.1.
- 1163 Schmidt, J., Hacker, B.R., Ratschbacher, L., Stübner, K., Stearns, M., Kylander-Clark, A., Cottle,
- J.M., Alexander, A., Webb, G., Gehrels, G., and Minaev, V., 2011, Cenozoic deep crust in
- the Pamir: Earth and Planetary Science Letters, v. 312, p. 411-421, doi:
- 1166 10.1016/j.epsl.2011.10.034.
- 1167 Schwab, M., Ratschbacher, L., Siebel, W., McWilliams, M., Minaev, V., Lutkov, V., Chen, F.,
- Stanek, K., Nelson, B., Frisch, W., and Wooden, J.L., 2004, Assembly of the Pamirs: Age
- and origin of magmatic belts from the southern Tien Shan to the southern Pamirs and their
- relation to Tibet: Tectonics, v. 23, doi: 10.1029/2003tc001583.
- Siehl, A., 2015, Structural setting and evolution of the Afghan orogenic segment-A Review:
- Geological Society, London, Special Publications, v. 427, p. 57–88, doi: 10.1144/sp427.8.
- Sláma, J., Košler, J., Condon, D.J., Crowley, J.L., Gerdes, A., Hanchar, J.M., Horstwood, M.S.A.,
- Morris, G.A., Nasdala, L., Norberg, N., Schaltegger, U., Schoene, B., Tubrett, M.N., and
- Whitehouse, M.J., 2008, Plešovice zircon a new natural reference material for U-Pb and
- 1176 HF isotopic microanalysis: Chemical Geology, v. 249, p. 1–35, doi:
- 1177 10.1016/j.chemgeo.2007.11.005.
- Sobel, E.R., and Dumitru, T.A., 1997, Thrusting and exhumation around the margins of the
- western Tarim basin during the India-Asia collision: Journal of Geophysical Research: Solid
- Earth, v. 102, p. 5043–5063, doi: 10.1029/96jb03267.

- Sobel, E.R., 1999, Basin analysis of the Jurassic-Lower Cretaceous southwest Tarim basin,
- Northwest China: Geological Society of America Bulletin, v. 111, p. 709-724, doi:
- 1183 10.1130/0016-7606(1999)111<0709:baotjl>2.3.co;2.
- Sobel, E.R., Chen, J., Schoenbohm, L.M., Thiede, R., Stockli, D.F., Sudo, M., and Strecker, M.R.,
- 1185 2013, Oceanic-style subduction controls late Cenozoic deformation of the Northern Pamir
- orogen: Earth and Planetary Science Letters, v. 363, p. 204-218, doi:
- 1187 10.1016/j.epsl.2012.12.009.
- Song, Z.H., Zhang, C.L., Sargazi, M., Hussain, Z., Liu, X.Q., Ye, X.T., and Wang, H.R., 2024,
- 1189 Carboniferous bimodal volcanic sequences along the northeastern Pamir: Evidence for back-
- arc extension due to northward subduction of the paleo-tethys: Geological Society of America
- 1191 Bulletin, doi: 10.1130/b37153.1.
- Stevens, T., Carter, A., Watson, T.P., Vermeesch, P., Andò, S., Bird, A.F., Lu, H., Garzanti, E.,
- 1193 Cottam, M.A., and Sevastjanova, I., 2013, Genetic linkage between the Yellow River, the Mu
- 1194 Us desert and the Chinese Loess Plateau: Quaternary Science Reviews, v. 78, p. 355–368,
- doi: 10.1016/j.guascirev.2012.11.032.
- Sun, F., 1989, Early and Middle Jurassic sporo-pollen assemblages of Quiquanhu coal field of
- Turpan, Xinjiang: Acta Botanica Sinica, v. 31, p. 638–646.
- Tang, G.J., Cawood, P.A., Wyman, D.A., Dan, W., Wang, Q., and Yang, Y.N., 2021, The missing
- magmatic arc in a long-lived ocean from the Western Kunlun–Pamir Paleo-Tethys realm:
- 1200 Geophysical Research Letters, v. 48, doi: 10.1029/2021gl095192.
- 1201 Tian, Z., Chai, G., and Kang, Y., 1989, Tectonic evolution of the Tarim basin, in Chinese
- Sedimentary Basins: in: Zhu, X., eds., Sedimentary Basins of the World, Elsevier,
- 1203 Amsterdam, p. 33–42.

- 1204 Torsvik, T.H., and Cocks, L.R., 2013, Gondwana from top to base in space and time: Gondwana
- 1205 Research, v. 24, p. 999–1030, doi: 10.1016/j.gr.2013.06.012.
- 1206 Vermeesch, P., 2013, Multi-sample comparison of detrital age distributions: Chemical Geology,
- v. 341, p. 140–146, doi: 10.1016/j.chemgeo.2013.01.010.
- 1208 Villarreal, D.P., Robinson, A.C., Carrapa, B., Worthington, J., Chapman, J.B., Oimahmadov, I.,
- Gadoev, M., and MacDonald, B., 2020, Evidence for Late Triassic crustal suturing of the
- 1210 Central and Southern Pamir: Journal of Asian Earth Sciences: X, v. 3, p. 100024, doi:
- 1211 10.1016/j.jaesx.2019.100024.
- 1212 Villarreal, D.P., Robinson, A.C., Chapman, J.B., Carrapa, B., Oimuhammadzoda, I., Gadoev, M.,
- and Li, Y., 2023, Early Cretaceous displacement on the Tanymas thrust fault, Northern Pamir,
- Tajikistan, and regional tectonic implications: Journal of Asian Earth Sciences: X, v. 9, p.
- 1215 100147, doi: 10.1016/j.jaesx.2023.100147.
- von Eynatten, H., and Dunkl, I., 2012, Assessing the sediment factory: The role of single grain
- analysis: Earth-Science Reviews, v. 115, p. 97–120, doi: 10.1016/j.earscirev.2012.08.001.
- Wang, J., Hattori, K., Liu, J.G., Song, Y., Gao, Y.B., and Zhang, H., 2017, Shoshonitic- and
- adakitic magmatism of the Early Paleozoic age in the Western Kunlun orogenic belt, NW
- 1220 China: Implications for the early evolution of the northwestern Tibetan plateau: Lithos, v.
- 1221 286–287, p. 345–362, doi: 10.1016/j.lithos.2017.06.013.
- Wang, S.F., Tang, W.K., Liu, Y.D., Liu, X.H., and Yao, X., 2020, Rushan-Pshart Paleo-Tethyan
- suture deduced from geochronological, geochemical, and Sr–Nd–HF isotopic characteristics
- of granitoids in Pamir: Lithos, v. 364–365, p. 105549, doi: 10.1016/j.lithos.2020.105549.

- Weltje, G.J., von Eynatten, H., 2004, Quantitative provenance analysis of sediments: an
- introduction, in: Weltje, G.J., and von Eynatten, H., eds., Quantitative Provenance Analysis
- of Sediments: Sedimentary Geology, p. 1–11.
- Williams, I.S., 2001, Response of detrital zircon and monazite, and their U–Pb isotopic systems,
- to regional metamorphism and host rock partial melting, Cooma Complex, southeastern
- Australia: Australian Journal of Earth Sciences, v. 48, p. 557-580, doi: 10.1046/j.1440-
- 1231 0952.2001.00883.x.
- Windley, B., 1983, Metamorphism and tectonics of the Himalaya: Journal of the Geological
- 1233 Society, v. 140, p. 849–865, doi: 10.1144/gsjgs.140.6.0849.
- Wolfart, R., and Wittekindt, H., 1980, Geologie von Afghanistan: von Reinhard Wolfart u.
- Hanspeter Wittekindt, Borntraeger, Berlin, Stuttgart.
- Wolf, S.G., Huismans, R.S., Braun, J., and Yuan, X.P., 2022, Topography of mountain belts
- 1237 controlled by rheology and surface processes: Nature, v. 606, p. 516-521, doi:
- 1238 10.1038/s41586-022-04700-6.
- Worthington, J.R., Ratschbacher, L., Stübner, K., Khan, J., Malz, N., Schneider, S., Kapp, P.,
- 1240 Chapman, J.B., Stevens Goddard, A., Brooks, H.L., Lamadrid, H.M., Steele-MacInnis, M.,
- Rutte, D., Jonckheere, R., Pfänder, J., Hacker, B.R., Oimahmadov, I., Gadoev, M., 2020, The
- 1242 Alichur Dome, South Pamir, Western India-Asia collisional zone: Detailing the Neogene
- Shakhdara–Alichur syn-collisional gneiss-dome complex and connection to lithospheric
- processes: Tectonics, v. 39, doi: 10.1029/2019tc005735.
- Wu, F.Y., Wan, B., Zhao, L., Xiao, W.J., and Zhu, R.X., 2020, Tethyan geodynamics: Acta
- Petrologica Sinica, v. 36, p. 1637–1674, doi: 10.18654/1000-0569/2020.06.01.

- Wu, H.X., 2017, Characteristics of paleostructure in the mountain front region of south-western
- Tarim Basin and its control of Jurassic-Cretaceous deposition [M.S. thesis]: Hangzhou,
- 1249 China, Zhejiang University.
- Wu, H.X., Chen, H.L., Zuza, A.V., Dilek, Y., Qiu, D.W., Lu, Q.Y., Zhang, F.Q., Cheng, X.G., and
- Lin, X.B., 2024, Alternating extensional and contractional tectonics in the West Kunlun
- Mountains during Jurassic: Responses to the Neo-Tethyan geodynamics along the Eurasian
- margin, EGUsphere [preprint], doi: 10.5194/egusphere-2024-1670, 2024.
- 1254 Wu, H.X., Cheng, X.G., Chen, H.L., Chen, C., Dilek, Y., Shi, J., Zeng, C.M., Li, C.Y., Zhang, W.,
- Zhang, Y.Q., Lin, X.B., and Zhang, F.Q., 2021, Tectonic switch from Triassic contraction to
- Jurassic-Cretaceous extension in the Western Tarim Basin, Northwest China: New insights
- into the evolution of the Paleo-Tethyan Orogenic Belt. Frontiers in Earth Science, v. 9, doi:
- 1258 10.3389/feart.2021.636383.
- 1259 Xiao, L., Zhang, H.F., Clemens, J.D., Wang, Q.W., Kan, Z.Z., Wang, K.M., Ni, P.Z., and Liu,
- 1260 X.M., 2007, Late Triassic granitoids of the eastern margin of the Tibetan Plateau:
- Geochronology, petrogenesis and implications for tectonic evolution: Lithos, v. 96, p. 436–
- 1262 452, doi: 10.1016/j.lithos.2006.11.011.
- 1263 Xiao, W.J., Windley, B.F., Chen, H.L., Zhang, G.C., and Li, J.L., 2002, Carboniferous–Triassic
- subduction and accretion in the western Kunlun, China: Implications for the collisional and
- accretionary tectonics of the northern Tibetan Plateau: Geology, v. 30, p. 295, doi:
- 1266 10.1130/0091-7613(2002)030<0295:ctsaai>2.0.co;2.
- 1267 Xiao, W.J., Han, F.L., Windley, B.F., Yuan, C., Zhou, H., and Li, J.L., 2003, Multiple accretionary
- orogenesis and episodic growth of continents: Insights from the Western Kunlun Range,

- 1269 Central Asia: International Geology Review, v. 45, p. 303–328, doi: 10.2747/0020-
- 1270 6814.45.4.303.
- 1271 Xu, Q., Zhao, J.M., Yuan, X.H., Liu, H.B., Ju, C.H., Schurr, B., and Bloch, W., 2021, Deep crustal
- contact between the Pamir and Tarim Basin deduced from receiver functions: Geophysical
- 1273 Research Letters, v. 48, doi: 10.1029/2021gl093271.
- 1274 Xu, W., Dong, Y.S., Zhang, X.Z., Deng, M.R., and Zhang, L., 2016, Petrogenesis of high-Ti mafic
- dykes from Southern Qiangtang, Tibet: Implications for a ca. 290 Ma large igneous province
- related to the early Permian rifting of Gondwana: Gondwana Research, v. 36, p. 410–422,
- 1277 doi: 10.1016/j.gr.2015.07.016.
- 1278 Xu, W., Liu, F.L., and Dong, Y.S., 2020, Cambrian to Triassic geodynamic evolution of central
- 1279 Qiangtang, Tibet: Earth-Science Reviews, v. 201, p. 103083, doi:
- 1280 10.1016/j.earscirev.2020.103083.
- 1281 Yan, Q.H., Wang, H., Chi, G.X., Wang, Q., Hu, H., Zhou, K.L., and Zhang, X.Y., 2022,
- Recognition of a 600-km-long Late Triassic rare metal (Li-Rb-Be-Nb-Ta) pegmatite belt in
- the western Kunlun Orogenic Belt, western China: Economic Geology, v. 117, p. 213–236,
- doi: 10.5382/econgeo.4858.
- 1285 Yang, W., Fu, L., Wu, C.D., Song, Y., Jiang, Z.X., Luo, Q., Zhang, Z.Y., Zhang, C., and Zhu, B.,
- 1286 2018, U-Pb ages of detrital zircon from Cenozoic sediments in the south-western Tarim
- Basin, NW China: Implications for Eocene-Pliocene source-to-sink relations and new
- insights into Cretaceous–Paleogene magmatic sources: Journal of Asian Earth Sciences, v.
- 1289 156, p. 26–40, doi: 10.1016/j.jseaes.2018.01.010.

- 1290 Yin, A., and Harrison, T.M., 2000, Geologic evolution of the Himalayan-Tibetan orogen: Annual
- Review of Earth and Planetary Sciences, v. 28, p. 211-280, doi:
- 1292 10.1146/annurev.earth.28.1.211.
- 1293 Yin, J.Y., Xiao, W.J., Sun, M., Chen, W., Yuan, C., Zhang, Y.Y., Wang, T., Du, Q., Wang, X.S.,
- and Xia, X.P., 2020, Petrogenesis of Early Cambrian granitoids in the western Kunlun
- orogenic belt, Northwest Tibet: Insight into early stage subduction of the Proto-Tethys Ocean:
- Geological Society of America Bulletin, v. 132, p. 2221–2240, doi: 10.1130/b35408.1.
- Yuan, C., Sun, M., Zhou, M.F., Zhou, H., Xiao, W.J., and Li, J.L., 2002, Tectonic evolution of the
- west Kunlun: Geochronologic and geochemical constraints from Kudi granitoids:
- 1299 International Geology Review, v. 44, p. 653–669, doi: 10.2747/0020-6814.44.7.653.
- Zanchetta, S., Worthington, J., Angiolini, L., Leven, E.Ja., Villa, I.M., and Zanchi, A., 2018, The
- Bashgumbaz Complex (Tajikistan): Arc obduction in the Cimmerian orogeny of the Pamir:
- Gondwana Research, v. 57, p. 170–190, doi: 10.1016/j.gr.2018.01.009.
- 1303 Zha, X.F., Dong, Y.P., Gao, X.F., Ji, W.H., Liu, X.M., He, D.F., Li, P., Zhang, H.D., and Yang,
- 1304 C., 2022, The Early Paleozoic Subashi ophiolite in the West Kunlun Orogenic Belt
- 1305 (northwestern Tibetan Plateau): Implication for the tectonic evolution of the Proto-Tethys:
- Journal of Asian Earth Sciences, v. 238, doi.org/10.1016/j.jseaes.2022.105388.
- Zhang, C.L., Yu, H.F., Ye, H.M., Zhao, Y., and Zhang, D.S., 2006, Aoyitake plagiogranite in
- western Tarim Block, NW China: Age, geochemistry, Petrogenesis and its tectonic
- implications: Science in China Series D: Earth Sciences, v. 49, p. 1121–1134, doi:
- 1310 10.1007/s11430-006-1121-y.

- Zhang, C.L., Zou, H.B., Ye, X.T., and Chen, X.Y., 2018, A newly identified Precambrian terrane
- at the Pamir Plateau: The Archean basement and Neoproterozoic granitic intrusions:
- Precambrian Research, v. 304, p. 73–87, doi: 10.1016/j.precamres.2017.11.006.
- Zhang, C.L., Zou, H.B., Ye, X.T., and Chen, X.Y., 2019a, Tectonic evolution of the West Kunlun
- Orogenic Belt along the northern margin of the Tibetan Plateau: Implications for the assembly
- of the Tarim terrane to Gondwana: Geoscience Frontiers, v. 10, p. 973–988, doi:
- 1317 10.1016/j.gsf.2018.05.006.
- 1318 Zhang, Q.C., Li, Z.H., Wu, Z.H., Chen, X.H., Zhang, J.E., and Yang, Y., 2021, Subduction
- initiation of the western Proto-Tethys Ocean: New evidence from the Cambrian intra-oceanic
- forearc ophiolitic mélange in the western Kunlun Orogen, NW Tibetan Plateau: Geological
- Society of America Bulletin, v. 134, p. 145–159, doi.org/10.1130/B35922.1.
- Zhang, S.J., Hu, X.M., and Garzanti, E., 2019b, Paleocene initial indentation and early growth of
- the Pamir as recorded in the western Tarim Basin: Tectonophysics, v. 772, p. 228207, doi:
- 1324 10.1016/j.tecto.2019.228207.
- 1325 Zheng, J.P., and Dai, H.K., 2018, Subduction and retreating of the western Pacific plate resulted
- in lithospheric mantle replacement and coupled basin-mountain respond in the North China
- 1327 Craton: Science China Earth Sciences, v. 61, p. 406–424, doi: 10.1007/s11430-017-9166-8.
- Zheng, Y.L., Wang, G.H., Guo, Z.W., Liang, X., Yuan, G.L., Wang, H.D., Huang, B., and He,
- Y.D., 2015, The record of the Pan-African and the Indosinian tectono-thermal event in
- Qiangtang terrane, northern Tibet: evidence from geochemical characteristics and U-Pb
- geochronology of the metamorphic complex in Ejiumai area: Acta Petrologicas Sinica, v. 31,
- p.1137–1152.

Zhong, D,K., Zhu, X.M., Wang, G.W., and Xie, Q.B., 2002, Paleoenvironments of Jurassic of

Kashi Sag in Tarim Basin: Journal of Palaeogeography, v. 4, p.47–54.

1335 Zhu, G.Y., Su, J., Yang, H.J., Wang, Y., Fei, A.G., Liu, K.Y., Zhu, Y.F., Hu, J.F., and Zhang, B.S.,

2013, Formation mechanisms of secondary hydrocarbon pools in the Triassic reservoirs in

the northern Tarim Basin: Marine and Petroleum Geology, v. 46, p. 51-66, doi:

10.1016/j.marpetgeo.2013.06.006.

FIGURE CAPTIONS

Figure 1. (A) Regional map of central Asia, illustrating the Western Kunlun Shan–Pamir Realm in relation to the Tibetan Plateau and India, along with the positions of significant basins, tectonic boundaries, and faults (adapted from Schwab et al., 2004; Robinson et al., 2007; Bershaw et al., 2012). (B) The geologic map of the Western Kunlun Shan–Pamir Realm and Tarim Basin, delineating various tectonic terranes, plutons, clastic deposits, as well as suture zones, modern river systems, and sampling localities (modified from Schwab et al., 2004; Chapman et al., 2018a; Zhang et al., 2019b). The lower left corner features three detailed geological maps centered on the locations of the three investigated sections: (C) Qimgan; (D) Oytag; (E) Toyunduk–Kyzyltau (modified from Zhang et al., 2019b; Rembe et al., 2022).

Figure 2. (A) The present tectonic framework of the Western Kunlun–Pamir Paleo-Tethys Realm with the prominent suture zones (adapted from Zanchetta et al., 2018). (B) Stratigraphic classification and the associated depositional environments of Jurassic strata within the southwestern Tarim Basin, as delineated by Sobel (1999) and Rembe et al. (2022). Triassic strata are largely absent, with only a few sections where they can be observed. A parallel unconformity contact is observed within the J_2t – J_3k strata and the overlying Jurassic and Cretaceous strata. J_1s :

1356 Shalitashi Formation; J₁k: Kangsu Formation; J₂y: Yangye Formation; J₂t: Targa Formation; J₃k: 1357 Kuzigongsu Formation; K1: Keziluse Group. 1358 Figure 3. (A) Composite stratigraphic section of the Jurassic strata at the Qimgan section. Refer 1359 to Figure 1B for the location of the Qimgan section. Stars, triangles, and squares indicate the 1360 approximate stratigraphic positions of each zircon U-Pb sample, thin section sample, and heavy 1361 mineral sample, respectively. (B) Longitudinal profile exhibiting couplets of structureless coarse-1362 grained cobble and indistinct cross-bedding fine-cobble/coarse-pebble conglomerates. (C) 1363 Parallel-bedded pebbly sandstone and coal-bearing mudstone, interpreted as braided river and 1364 floodplain deposits. (D) Parallel-bedded coarse to medium-grained sandstone and coarse-pebble 1365 conglomerate. (E) Light-gray siltstone and purple brown siltstone, interpreted as delta front or 1366 shallow lacustrine deposits. (F) Coarse-grained high-temperature quartz. Sample QM-10, XPL. (G) Oscillatory zoning and corroded embayments of plagioclase. Sample QM-6, XPL. (H) Mafic 1367 1368 volcanic lithic. Sample QM-1, PPL. (I) Granite lithics. Sample QM-1, XPL. (J) Parallel 1369 unconformity between the J₂t, J₃k and Cretaceous strata at the Qimgan section. F: feldspar; PPL: 1370 plane-polarized light; Q: quartz; VF: volcanic lithics; XPL: cross-polarized light. The color coding corresponds to the lithological types depicted in the vertical section. 1371 1372 Figure 4. The results of point counting are presented on the Q-F-L and Lv-Lm-Ls (volcanic lithics-1373 metamorphic lithics-sedimentary lithics) triangular diagrams, as proposed by Garzanti (2019), 1374 alongside representative microscopic images of various sections and wells. (A) Qimgan secion; 1375 (B) Oytag section; (C) Toyunduk–Kyzyltau section; (D) Fusha region. F: feldspar; Fe=feldspathic; 1376 FL=feldspatho-lithic; fLQ=feldspatho-litho-quartzose; FQ=feldspatho-quartzose; 1377 fQL=feldspatho-quartzo-lithic; LF=litho-feldspathic; IFQ=litho-feldspatho-quartzose; Li=lithic; 1378 LQ=litho-quartzose; lQF=litho-quartzo-feldspathic; MF: metamorphic lithics; Q: quartz;

1380 lithofeldspathic; Ou=quartzose; VF: volcanic lithics. 1381 Figure 5. (A) Composite stratigraphic section of the Jurassic strata at the Oytag section. Refer to 1382 Figure 1B for the location of the Oytag section. (B) The angular unconformity that separates the 1383 Jurassic conglomerate from the underlying Triassic basalt. (C) Planar-interstratified coarse/fine-1384 pebble conglomerate, interpreted as alluvial fan deposits. (D) Interbedded coarse-grained 1385 sandstone and fine conglomerate with cross bedding, interpreted as channel deposits of alluvial 1386 fan. (E) The thick sequence of dull red mudstone and purple brown sandstone at the top of the 1387 Jurassic strata. (F) Monocrystal quartz grains characterized by a water-clear appearance, smooth 1388 surfaces, and a sharply angular habit. Sample OY-3, XPL. (G) Intermediate–felsic volcanic lithic. 1389 Sample OY-20, XPL. (H) Mafic-intermediate volcanic lithic. Sample OY-23, XPL. (I) granitoid 1390 lithic. Sample OY-11, XPL. AF: alluvial fan; C: calcite cements; F: feldspar; MF: metamorphic 1391 lithics; Q: quartz; VF: volcanic lithics; XPL: cross-polarized light. 1392 Figure 6. (A) Composite stratigraphic section of the Jurassic strata from the Toyunduk–Kyzyltau 1393 section. Refer to Figure 1B for the location of the Toyunduk-Kyzyltau section. (B) Interbedded 1394 sandstone and siltstone, interpreted as channel deposits of braided delta plain deposits. (C) 1395 Interbedded massive sandstone and laminated siltstone, interpreted as channel deposits of braided 1396 delta plain deposits. (D) Alternating layers of fine-grained clastic rock series in the J₂t strata of the 1397 Toyunduk-Kyzyltau section. (E) Ripples on the surface of sandstone. (F) Sequence of dull red 1398 conglomerate at the top of the Jurassic strata, interpreted as alluvial fan deposits. (G) Parallel 1399 unconformity between the Jurassic and Cretaceous at the Toyunduk–Kyzyltau section. (H) Quartz 1400 grains and metamorphic lithics with cloudy and rough surfaces. Sample TY-ks09, XPL. (I) Quartz 1401 grains and metamorphic lithics with cloudy and rough surfaces. Sample TY-ks07, XPL. (J)

qFL=quartzo-feldspatho-lithic; QL=quartzolithic;

qLF=quartzo-

1379

QF=quartzo-feldspathic;

1402 Frequent interbedding between coal seams and siltstones, hundreds of meters in thickness. BRD: 1403 braided river delta; M: matrix; MF: metamorphic lithics; O: quartz; XPL: cross-polarized light. 1404 Figure 7. Composite stratigraphic section of the Jurassic strata from (A) Well FS8, (B) Well FS9 1405 and (C) KY1 in Fusha Region. (D) The panel at right shows a detailed geological map around the 1406 Fusha Region. Reference for the location of the Fusha Region in Figure 1B. (E) Quartz grains are 1407 composed of monocrystalline grains and polycrystalline grains. Sample KY1-ts03, 714.0 m, XPL. 1408 (F) Microscopic features of quartz, metamorphic lithics, and matrix. Sample FS8-ts05, 3378.5 m, 1409 XPL. (G) Microscopic features of quartz and metamorphic lithics. Sample KY1-ts05, 706.0 m, 1410 XPL. F: feldspar; FD: fan delta; M: matrix; MF: metamorphic rock lithics; Q: quartz; XPL: cross-1411 polarized light. 1412 Figure 8. (A) Heatmap displaying the relative abundance of heavy minerals within the sandstone 1413 samples to facilitate optimal observation. Cluster analysis has identified two primary clusters: 1414 Cluster A (Qimgan and Oytag sections, n=6) and Cluster B (Toyunduk-Kyzyltau section and 1415 Fusha Rigion, n=12). Refer to Figure 3 and Figures 4–7 for the specific locations of the samples. 1416 (B) MDS plot of heavy minerals from the Jurassic sandstones. The stress value of 0.094 indicates 1417 a good fit. (C) Ternary plots for the tourmaline, garnet and epidote. (D) Provenance-sensitive 1418 heavy mineral index GZI (Morton and Hallsworth, 1994) displayed on the scatter plot. (E) 1419 Ultrastable heavy mineral index (ZTR; Hubert, 1962) displayed on the scatter plot. 1420 Figure 9. Cathodoluminescence (CL) images of representative zircon grains from the Jurassic 1421 sandstones. The red circles on the zircons indicate the analytical spots for U-Pb dating, while the 1422 numbers represent the corresponding U-Pb ages.

Figure 10. Th/U ratios of detrital zircon grains from age-dated Jurassic sandstone samples sourced

from the south-western Tarim Basin. Ratios exceeding 0.4 likely indicate an igneous origin (Corfu

1423

1424

- et al., 2003; Linnemann et al., 2011), whereas those below 0.1 are most likely linked to aqueous
- 1426 fluid-precipitated or metamorphic origins (Liati et al., 2002; Grant et al., 2009). Samples in the
- 1427 Toyunduk–Kyzyltau and Kandilik sections are from Wu et al. (2024).
- 1428 **Figure 11.** Normalized probability density plots for U-Pb detrital zircon data from modern rivers
- draining the Western Kunlun, South Pamir, Central Pamir, and North Pamir. The shaded bars
- highlight the *ca* 950–600 Ma (typical of Western Kunlun provenance of Proterozoic metamorphic
- 1431 crystalline basement), ca 510–380 Ma (typical of Western Kunlun provenance triggered by the
- 1432 closure of Proto-Tethys Ocean), ca 260-180 Ma (typical of Western Kunlun and North Pamir
- provenance triggered by the closure of Paleo-Tethys Ocean) and ca 120–70 Ma (typical of Pamir
- provenance triggered by the closure of Neo-Tethys Ocean). The peaks serve merely as a reference
- 1435 for the age distribution range, with no quantitative significance. References: (A, T–U)–Rittner et
- 1436 al. (2016); (B–C, L–N, S, V–W)–Blayney et al. (2016); (D–G, P, X, AA)–Carrapa et al. (2014);
- 1437 (H, Q-R, Z)-Liu et al. (2017); (I-K, O)-Lukens et al. (2012).
- 1438 **Figure 12.** Normalized probability density plots for U-Pb detrital zircon data from the Jurassic
- sandstones in south-western Tarim Basin are compared to the age probability curves from modern
- rivers draining the Western Kunlun, South Pamir, Central Pamir, and North Pamir. Data are from
- this study except where noted. Data sources: Sample PMR-25 is from Bershaw et al. (2012), and
- 1442 Samples KZLT1601, KZLT1602, ABYL13 are from Wu et al. (2024)
- 1443 Figure 13. Three-dimensional multidimensional scaling (3-D MDS) plots depicting the detrital-
- zircon age data from both Jurassic sandstones and modern-river sands that drain the Western
- 1445 Kunlun and North Pamir.
- 1446 **Figure 14.** Schematic diagrams delineating the synthesized depositional model of the Jurassic in
- the south-western Tarim Basin. The depocenters of the Jurassic basins generally trend north-

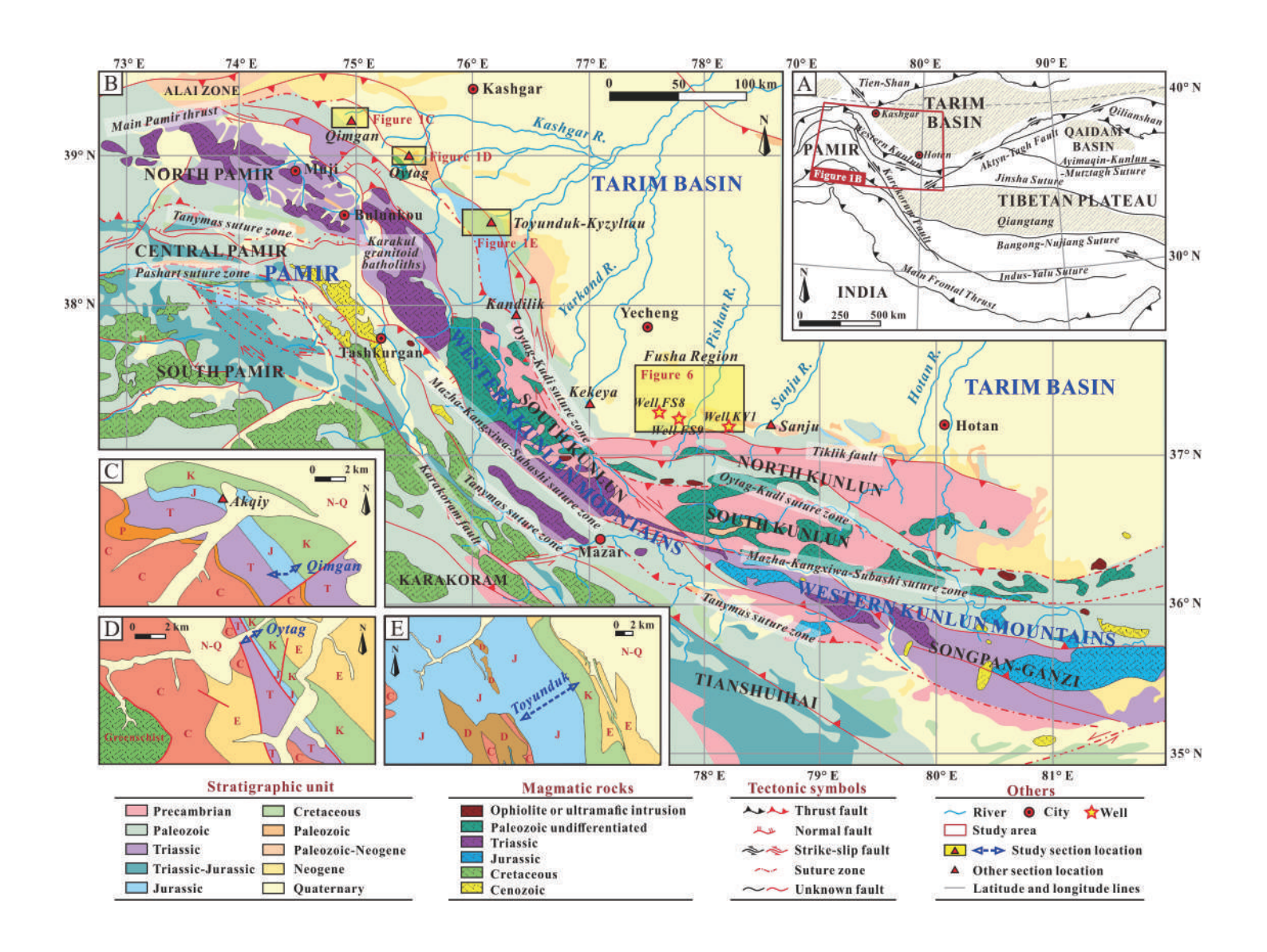
northwest, aligning subparallel to the axis of the Western Kunlun Shan–Pamir Realm. The westward drainage patterns, formed through headward erosion, evolved across the Western Kunlun Shan (WKS)–Pamir Realm. This figure is adapted from Wu (2017). It illustrates three stages of extension: (A) the initial stage, approximately corresponding to the J₁s and J₁k strata; (B) the fault linkage stage of extension, approximately corresponding to the J₂y and J₂t strata; and (C) the final stage of extension, approximately corresponding to the J₃k strata.

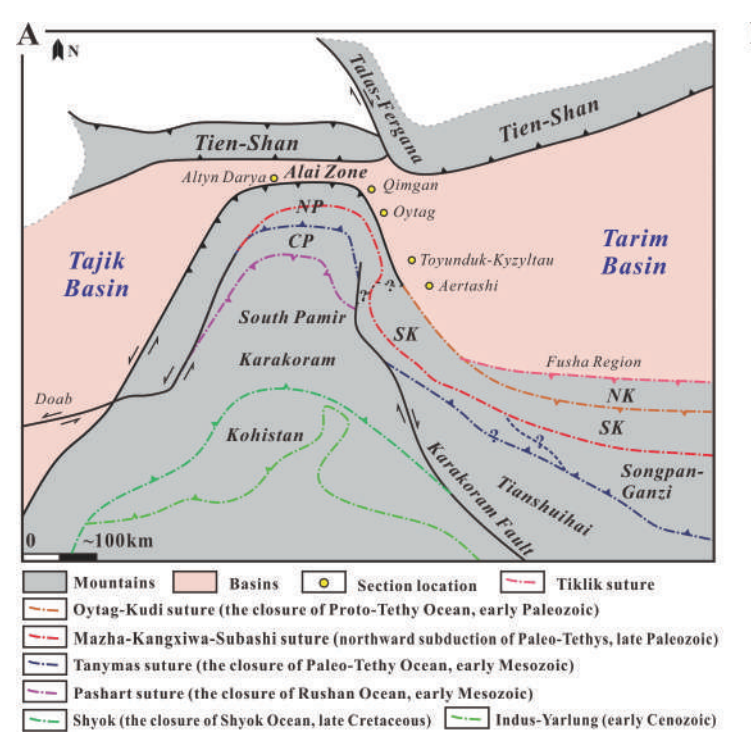
Figure 15. Schematic tectonic reconstructions illustrating the closure of the Western Kunlun–Pamir Paleo-Tethys Realm at key geological intervals, drawing inspiration from the works of Blayney et al. (2016), Yang et al. (2018), Li et al. (2020), and Aminov et al. (2023). The tectonic evolution encompassing the closure of the Western Kunlun–Pamir Paleo-Tethys Realm is conceptualized in three distinct phases: (A) the Carboniferous–Triassic pre-collision phase, (B) the Triassic syn-collision phase and (C) the Jurassic post-collisional phase. A comprehensive discussion of these phases is provided in the main text. C-PBV: Carboniferous–Permian bimodal volcanic sequence exposed along the north-eastern North Pamir; NK: North Kunlun Terrane; NP: North Pamir Terrane; SK: South Kunlun Terrane; SP-GZ: Songpan–Ganzi Terrane.

SUPPLEMENTAL MATERIAL

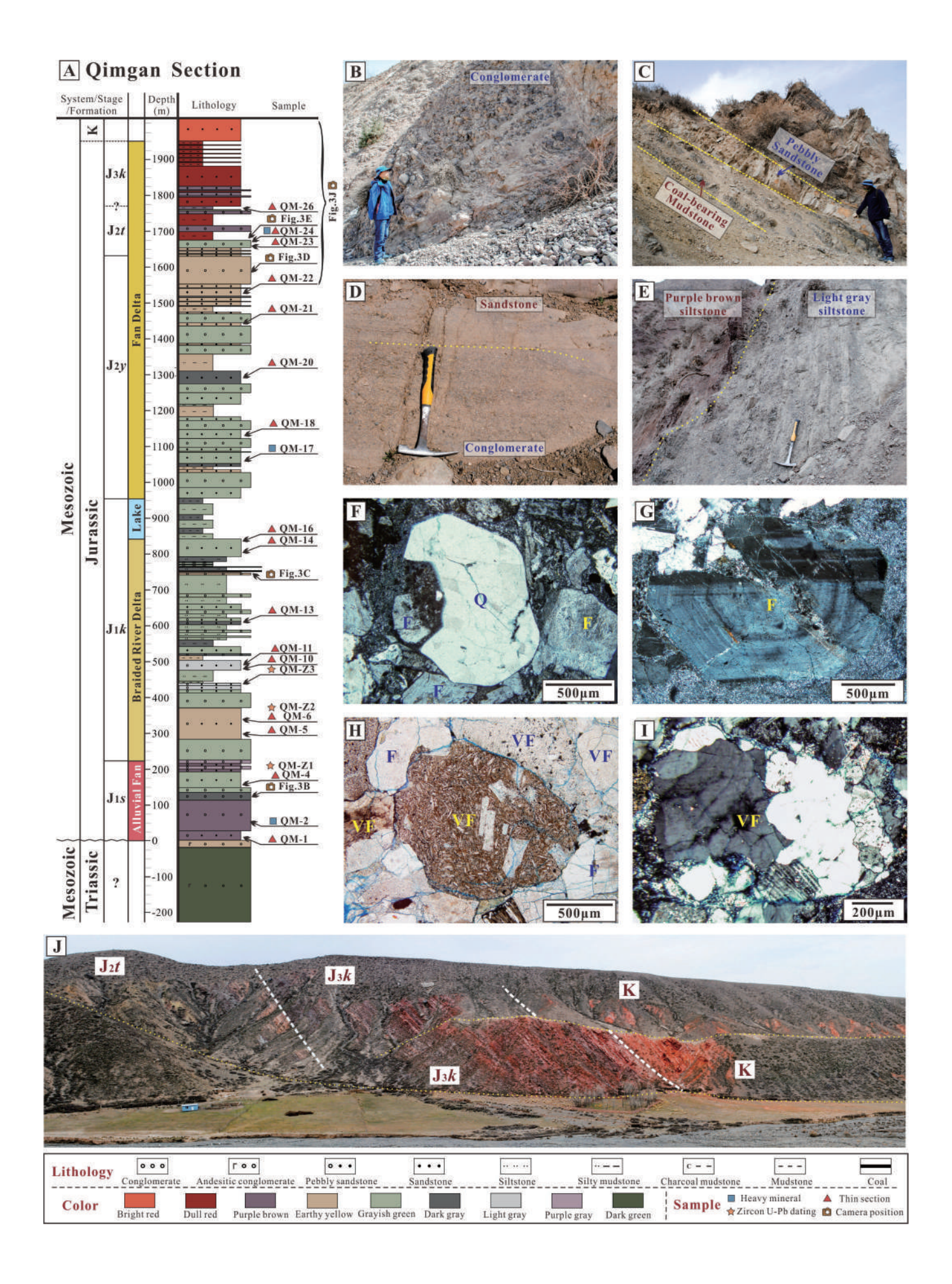
- **Appendix A.** Detailed sample collection information and section locations.
- **Appendix B.** Petrographic summary of Jurassic sandstones from the south-western Tarim Basin.
- 1467 Appendix C. Full Zircon U-Pb data set for Jurassic samples from south-western Tarim Basin.
- **Appendix D.** Sedimentological characteristics and environmental interpretation of Jurassic strata
- in the south-western Tarim Basin.

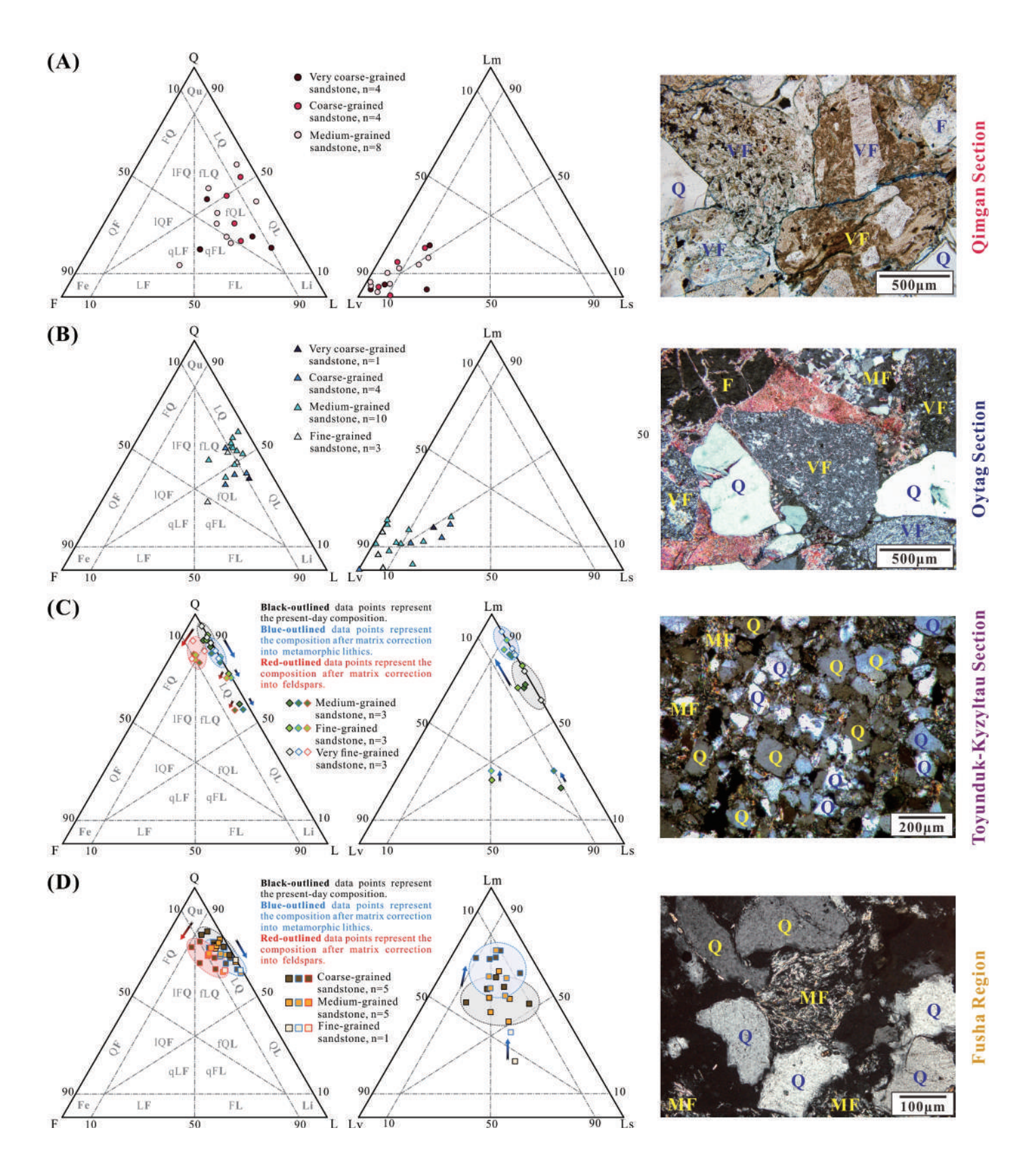
1470	Appendix E. Pollen statistics table from the Jurassic Aketao section in the south-western Tarim
1471	Basin.

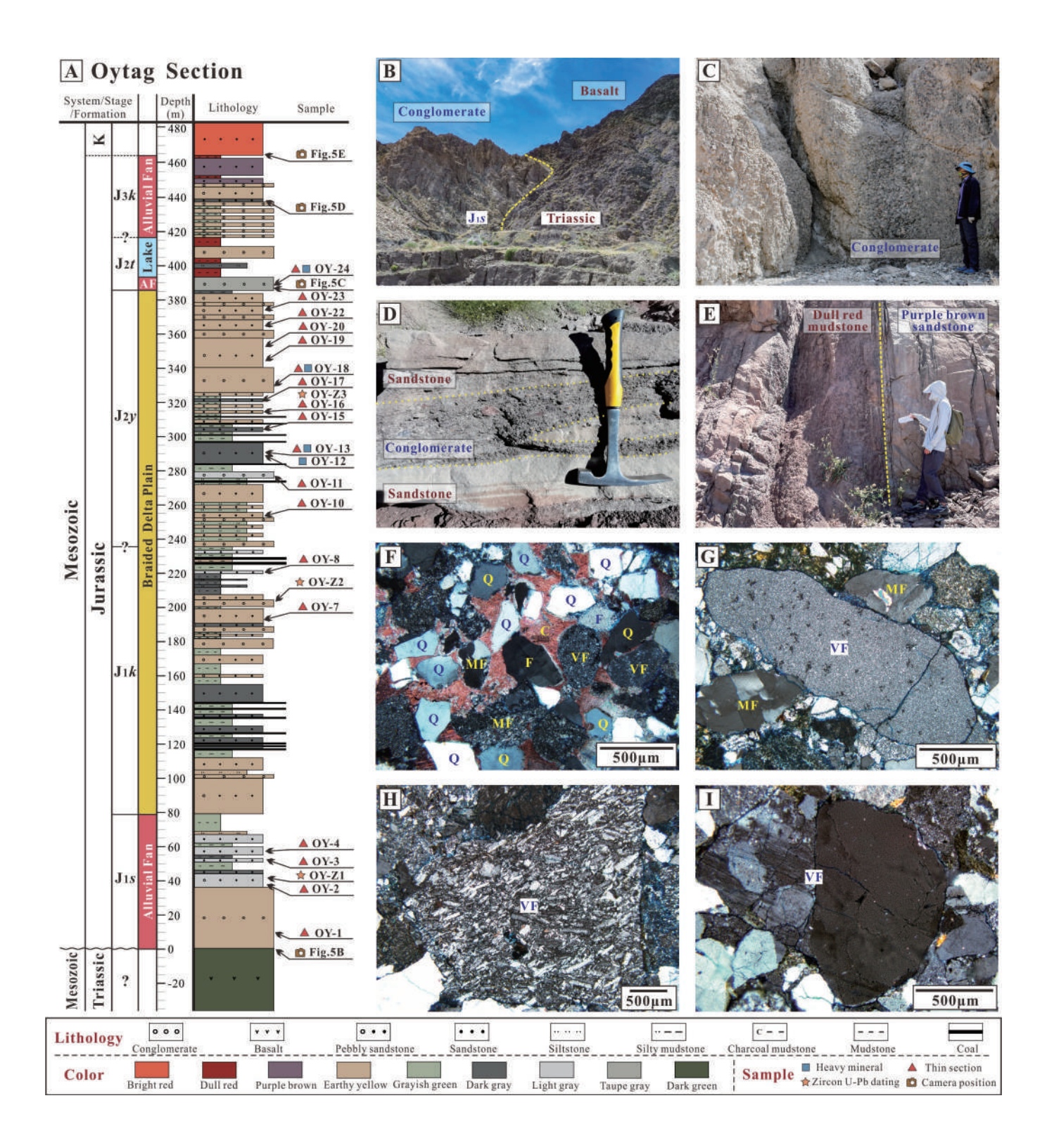


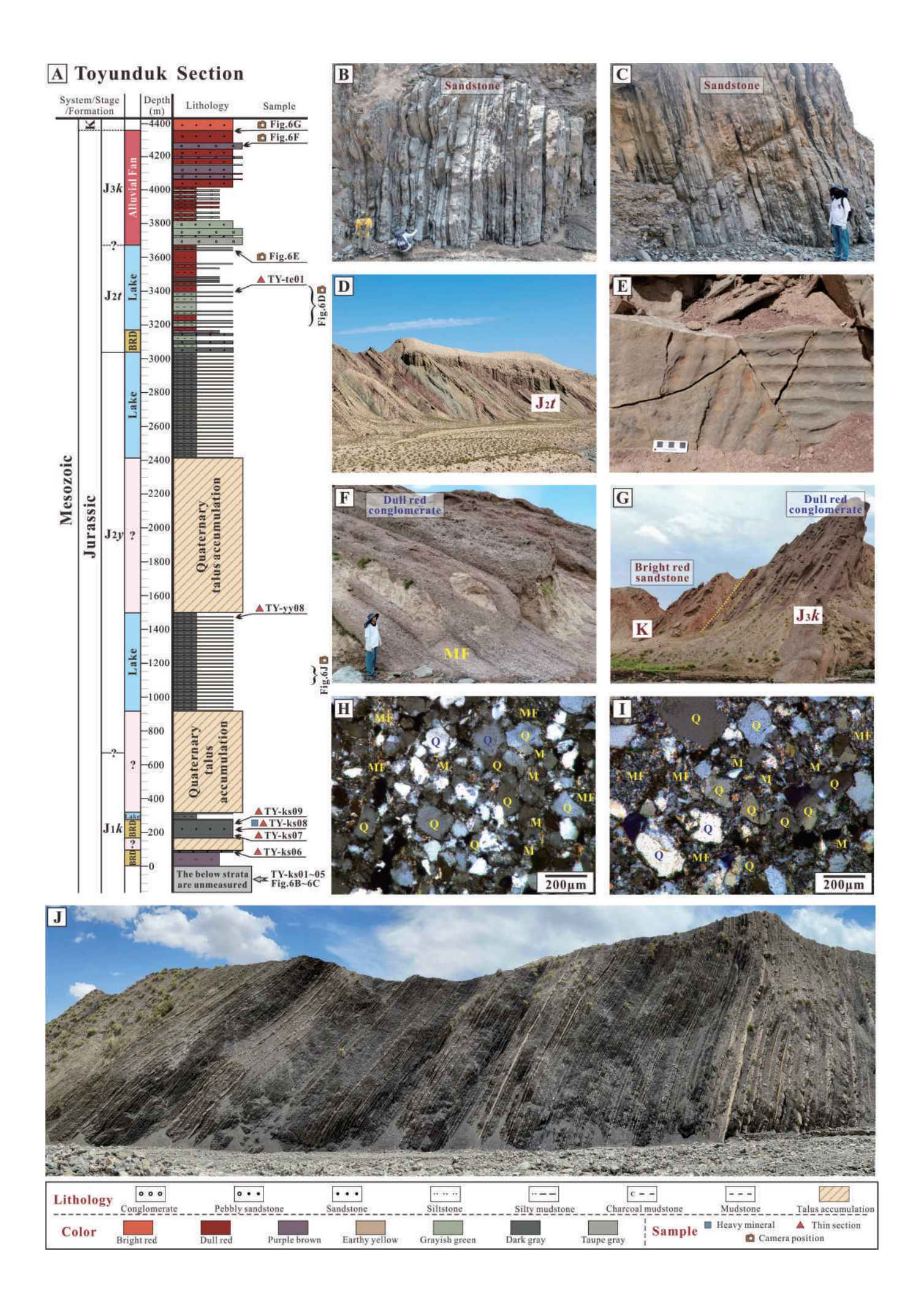


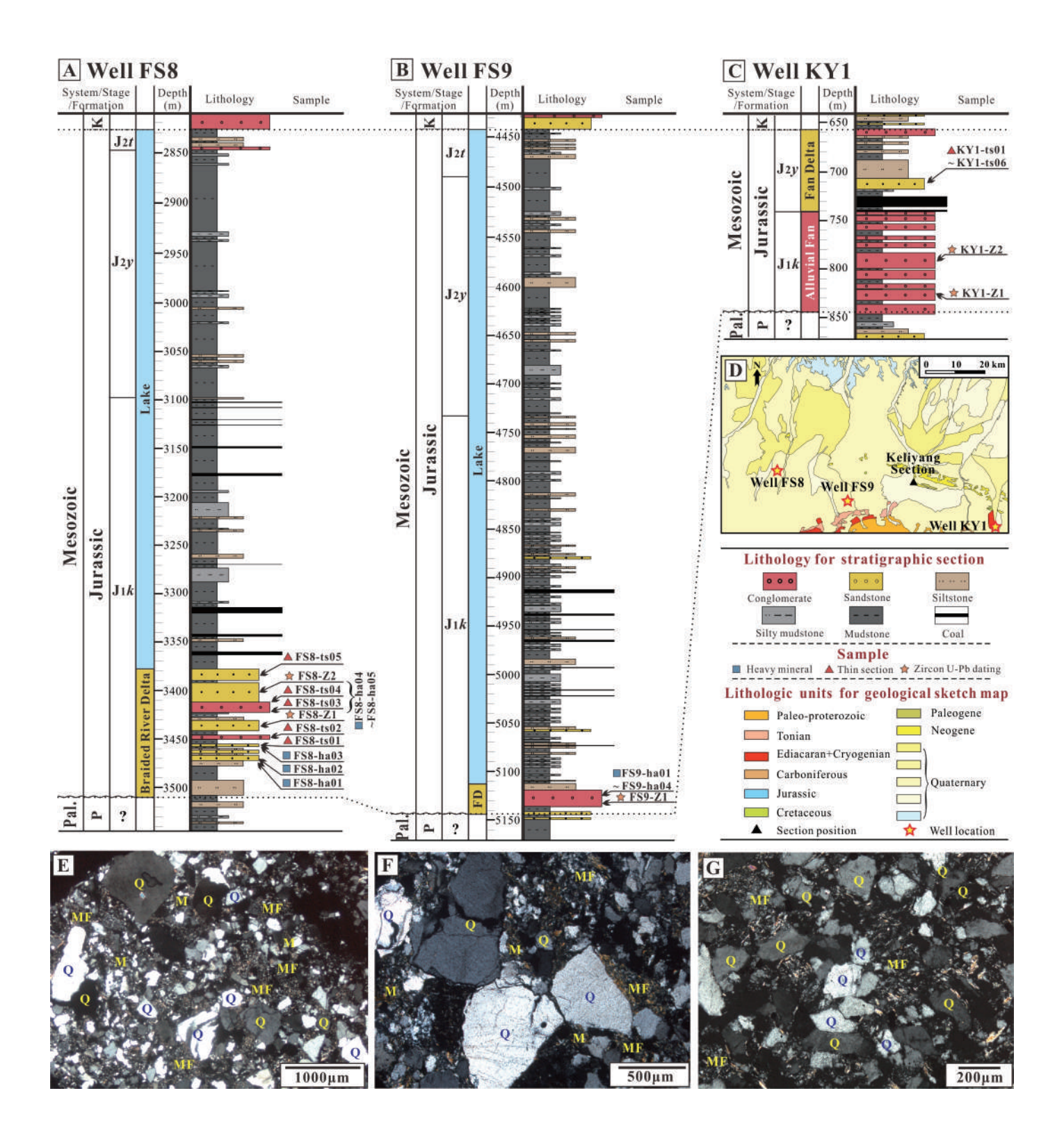
Age	e Unit		Unit		Depositional environments
Cre.	Kezilesu Group	K1k	Fluvial		
22	Kuzigongsu Fm.	J3k	Alluvial fan		
sic	Targa Fm.	J2 <i>t</i>	Shallow lacustrine		
Jurassic	Yangye Fm.	J2y	Swamp to lacustrine		
7	Kangsu Fm.	J1k	Fluvial to lacustrine		
	Shalitashi Fm.	Jis	Alluvial fan		
Triassic	Missing		Basaltic to andesit lava flow Sandstone, conglomerate, ignimbrite		

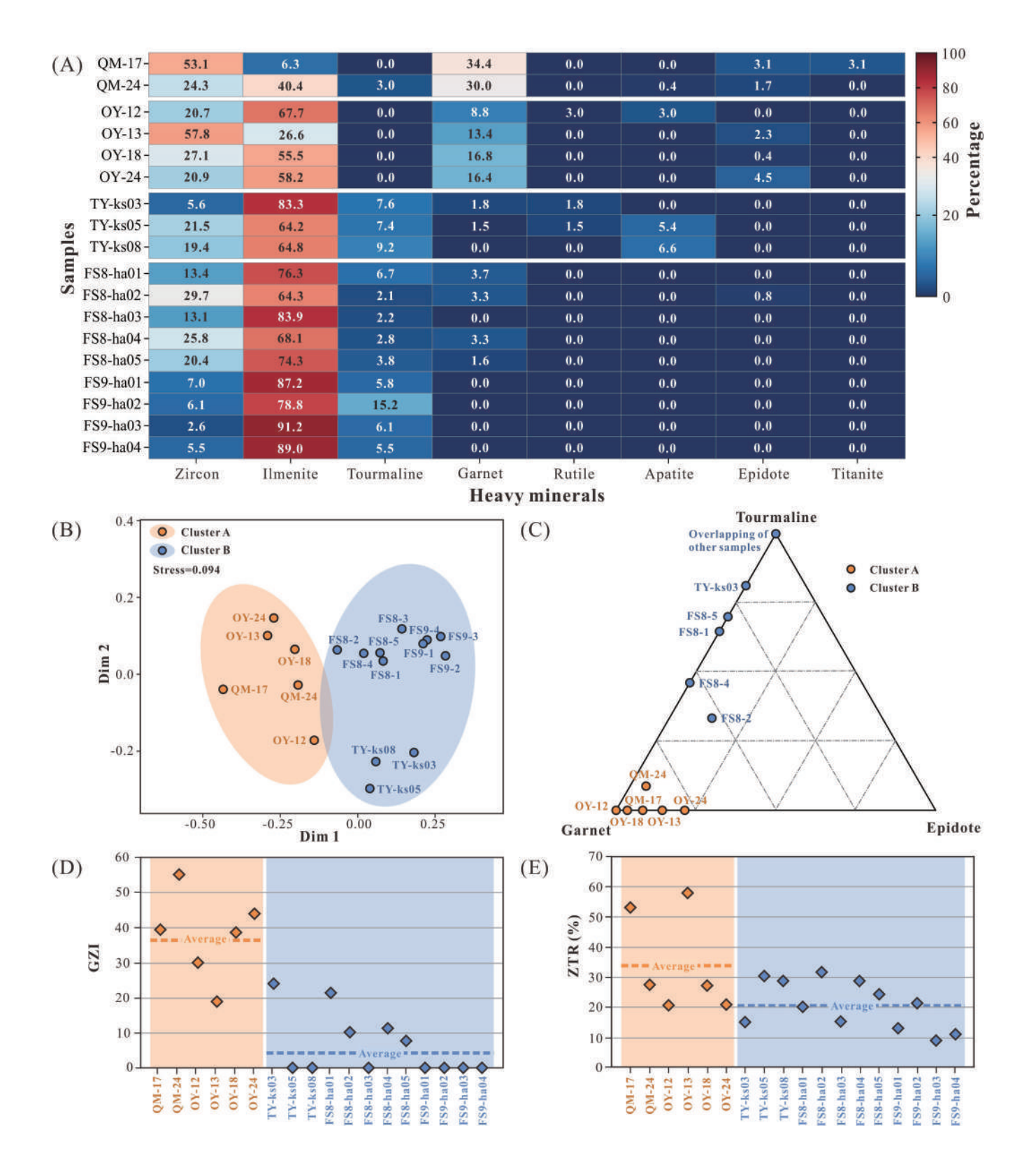




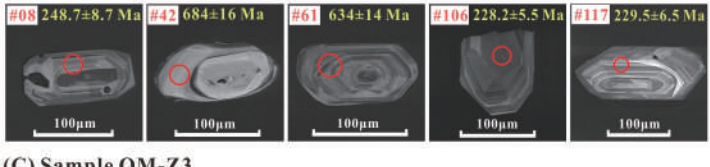




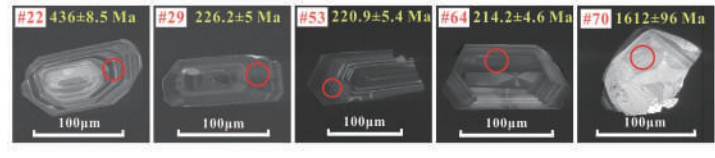




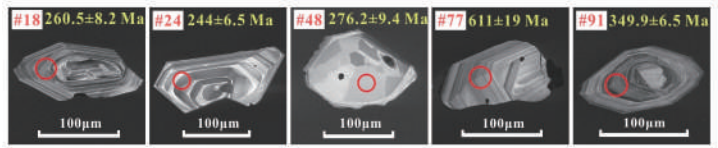
(A) Sample QM-Z1



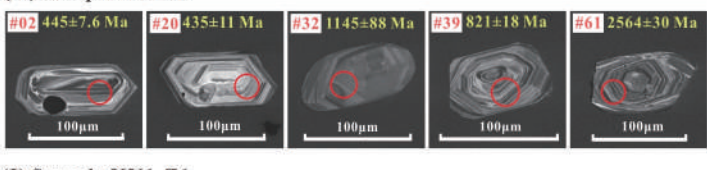
(C) Sample QM-Z3



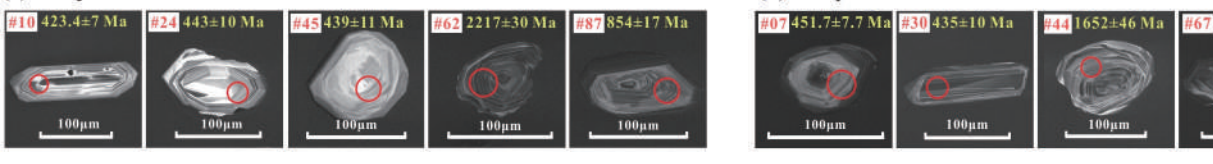
(E) Sample OY-Z2



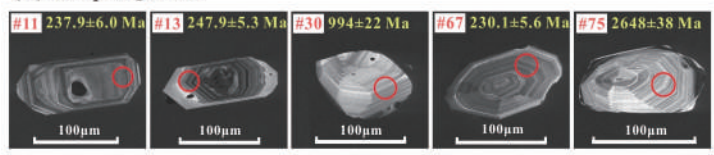
(G) Sample FS8-Z2



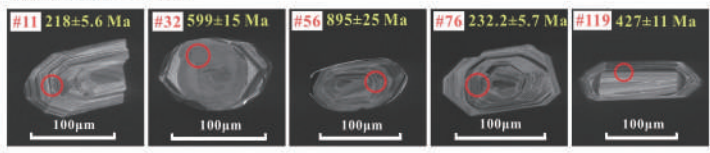
(I) Sample KY1-Z1



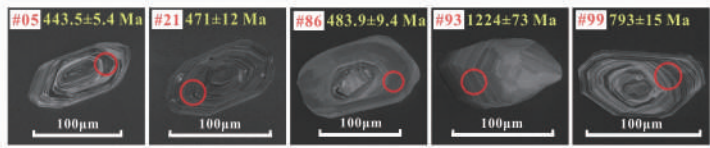
(B) Sample QM-Z2



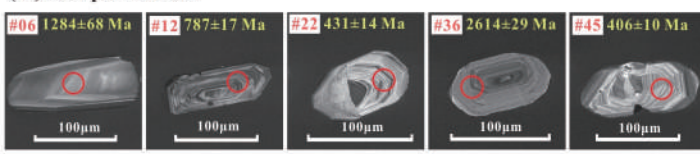
(D) Sample OY-Z1



(F) Sample FS8-Z1



(H) Sample FS9-Z1



(J) Sample KY1-Z2

